Journal of Marine Research, 55, 407–451, 1997

Journal of
MARINE RESEARCH

Volume 55, Number 3

The dynamics of an equivalent-barotropic model of the wind-driven circulation

by Pavel S. Berloff[1] and Stephen P. Meacham[1]

ABSTRACT

Various steady and time-dependent regimes of a quasi-geostrophic 1.5 layer model of an oceanic circulation driven by a steady wind stress are studied. After being discretized as a numerical model, the quasi-geostrophic equations of motion become a dynamical system with a large dimensional phase space. We find that, for a wide range of parameters, the large-time asymptotic regimes of the model correspond to low-dimensional attractors in this phase space. Motion on these attractors is significant in determining the intrinsic time scales of the system. In two sets of experiments, we explore the dependence of solutions on the viscosity coefficient and the deformation radius. Both experiments yielded a succession of solutions with different forms of time dependence including chaotic solutions. The transition to chaos in this model occurs through a modified classical Ruelle-Takens scenario. We computed some unstable steady regimes of the circulation and the associated fastest growing linear eigenmodes. The structure of the eigenmodes and the details of the energy conversion terms allow us to characterize the primary instability of the steady circulation. It is a complex instability of the western boundary intensification, the western gyre and the meander between the western and central gyres. The model exhibits ranges of parameters in which multiple, stable, time-dependent solutions exist. Further, we note that some bifurcations involve the appearance of variability at climatological time scales, purely as a result of the intrinsic dynamics of the wind-driven circulation.

1. Introduction

The main purpose of this research was to investigate the types of circulation regimes possible in a small, closed, rectangular basin and their dependence on different physical parameters, such as eddy viscosity, wind forcing and the basin's geometrical length scales,

1. Department of Oceanography, Florida State University, Tallahassee, Florida, 32306-3048, U.S.A.

with a view to understanding some of the mechanisms influencing the circulation in small inland seas.

Examples of almost-closed basins include the Mediterranean, Black, Red, Baltic and Caspian Seas. These bodies of water are *almost* closed in the sense that the straits connecting them with oceans are quite narrow.[2] Although the straits are very important for the formation of vertical stratification in the inner seas, dynamically, the basins are relatively isolated from main bodies of water. The shapes, sizes and circulation patterns of these basins are all different.

Observations (Oguz *et al.,* 1993) and some numerical simulations of the Black Sea (see Stanev, 1990; Meacham, 1997) suggest a rather complicated flow pattern with time-dependent and spatially variable mesoscale features like eddies and jets, but some robust flow features may be easily identified. Among them is the cyclonic Rim Current, flowing in a narrow band (its width is less than 75 km) around the periphery of the basin, along the continental slope, with typical alongshore surface velocities of about 0.2–0.3 m/sec. A series of eddies is confined between the coast and the Rim Current (Oguz *et al.,* 1993). These eddies are baroclinic features, anticyclonic above and cyclonic below the permanent thermocline. The Rim Current surrounds a basin-wide multi-centered cyclonic cell (Oguz *et al.,* 1993). The two dominant parts of the cyclonic cell are referred to in the literature as the Eastern and Western Gyres. The Gyres occupy the eastern and western parts of the Sea respectively, and one can see their shape and structure in Oguz *et al.*'s Figure 1. There is an associated elevation of isopycnals in the Gyre centers and depression of isopycnals around the basin's continental slopes. Observations (Blatov *et al.,* 1984) suggest that the Gyres are a time-dependent feature, and that they occur on an interannual time scale. An appearance of the Gyres is associated with an occasional breaking of the Rim Current into two closed loops, each of which surrounds one Gyre. This two-dome structure of the Gyres usually appears in summer, when cyclonic forcing is weaker. While some of the interannual variability in the Gyres is a result of variations in atmospheric forcing, we believe that some is a consequence of time scales intrinsic to the dynamics of the basin. Unfortunately, the lack of synoptic observational data is a major drawback in present studies of the mesoscale variability in the Sea.

From the existing observations, the circulation in the Black Sea is an interesting example of a phenomenon that exhibits large-scale organization. A sophisticated numerical model can simulate some of the basic features of the Sea circulation, but in this study the goal is to investigate the wind-driven circulation in a greatly simplified version of the Black Sea—a flat-bottomed, rectangular basin. This particular geophysical problem is an extension to the almost half-century old study of a wind-driven circulation in a closed basin pioneered by the works of Stommel (1948) and Munk (1950) on linear solutions of the barotropic vorticity equation.

Recently Jiang *et al.* (1995) discovered periodic solutions in the double-gyre wind-

2. The Caspian Sea has no direct connection with an ocean.

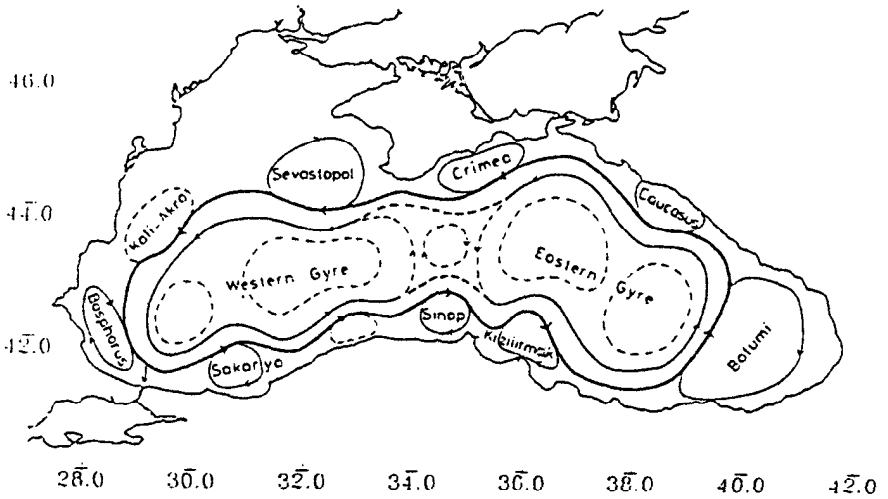

Figure 1. From Oguz *et al.* (1993). Schematic of the main features of the upper layer general circulation in the Black Sea. Solid (dashed) lines indicate quasi-permanent (recurrent) features of the circulation. Note the Rim Current flowing around the periphery of the basin and the Western and Eastern Gyres.

driven reduced-gravity shallow-water oceanic model. They concluded that periodic solutions arise by a Hopf bifurcation (i.e. an oscillatory instability and the nonlinear continuation of this instability; Drazin, 1992) from the steady state. Kamenkovich and Kamenkovich (1993) considered the evolution of frictionless Rossby waves generated by a wind stress in a closed basin. They demonstrated that a solution with a zero boundary value for the stream function fails to describe the wave motion in the basin, and that a consistent quasi-geostrophic formulation of the problem should include the total mass conservation constraint. As a result, interior Sverdrup flow may be obtained only in a time-average sense and, in the limit of zero friction, the Rossby wave oscillations do not decay with time. Ierley and Sheremet (1995) discovered multiple steady solutions in a barotropic single-gyre wind-driven model with slip boundary conditions on the lateral walls. The multiple solutions in that case exist in regimes in which the thickness of the inertial boundary layer, δ_I, is comparable to the thickness of the viscous boundary layer δ_M. One solution is characterized by the presence of the western boundary layer. In this case, the input of vorticity from the wind is balanced by the diffusion of vorticity with opposite sign from the western boundary. Another solution is an inertial-gyre circulation, characterized by large velocities and large vorticity gradients which are necessary for global vorticity balance. Velocities in the second type of solution are unrealistically large and this solution does not seem to be realized in the ocean. In addition to the pure antisymmetric solutions, asymmetric steady stable solutions were found in double-gyre antisymmetrically wind-driven reduced-gravity shallow-water (Jiang *et al.*, 1995) and barotropic (Cessi and Ierley, 1995) models. These solutions exist in pairs: strong cyclone and weak anticyclone, or vice

versa. Speich *et al.* (1995) showed that the multiple stationary solutions undergo Hopf bifurcations as the control parameters are varied, and eventually the flow becomes aperiodic and even chaotic. The chaotic behavior was related to an increased number of recirculations interacting with each other.

Starting with a very simple model, we try to simulate and explain the fundamental behavior of wind-driven flow in a small closed basin. We address the following questions. How does the circulation in the basin become unstable? What form do time-dependent solutions take and how do they behave in the parameter space? We solve numerically a discretized equation of motion. Before being discretized, it is a partial differential equation. When it is considered as a dynamical system, the phase space of the PDE is infinite dimensional. After discretization, we deal with a dynamical system of large but finite dimension (of the order of several thousand). The time-dependent evolution of the system from a given initial condition corresponds to a trajectory in this large-dimensional phase space.

The theory of forced, dissipative PDE's (e.g. Lions *et al.*, 1992; Robinson, 1995; Temam, 1995) suggests that the solution trajectories of equations similar to the nonlinear equivalent-barotropic vorticity equation, (2) below, should asymptotically tend to a finite dimensional attractor. Moreover, the expectation is that, in a sufficiently dissipative regime, the dimension of such an attractor should be relatively low. With this in mind, we pursue the following strategy.

We start from some arbitrarily chosen initial states and integrate the numerical model until the trajectory in the high dimensional phase space asymptotes to some attractor of a low dimension. We are interested in finding and classifying such asymptotic attractors for different values of the control parameters of the problem. Each low-dimensional attractor corresponds to a highly organized flow in physical space. An important issue is the extent of the ranges of the control parameters over which the system preserves its low dimensionality. We investigate bifurcation sequences that lead from steady states of the system to chaotic time-dependent behavior through several intermediate steps. The physics of the primary bifurcation is revealed by looking at the energy conversion associated with the growth of the most unstable eigenmode. An energy approach helps to localize an unstable part of the spatially nonuniform steady state circulation.

In this work, the focus is on a quasi-geostrophic reduced-gravity model; comparable calculations for barotropic and baroclinic flows are reported in Meacham and Berloff (1997, this issue) and Berloff and Meacham (1997a), respectively.

2. Modeling approach

In this research, we limit ourselves to a rectangular basin with 2 latitudinal and 2 meridional boundaries. We choose the y-axis to point northward, and the x-axis to point eastward. Basin sizes were chosen to be 800 km in the west-east direction (L_x) and 400 km in the south-north direction (L_y), which roughly corresponds to the horizontal scales of the Black Sea. We restrict the problem in hand to midlatitudes, and since the basin's length scales are much less than the Earth's radius, resort to a β-plane approximation. Thus, the

Coriolis parameter is $f = f_0 + \beta_0 y$, where $f_0 = .93 \times 10^{-4}$ sec^{-1}, $\beta_0 = 2 \times 10^{-11}$ m^{-1} sec^{-1} and $y = 0$ in the middle of the basin. No topographic forcing was included in the model and no thermohaline effects were considered. Instead a 1.5-layer model of stratification was used. In this model, only the upper layer is active. When at rest, the upper layer depth is H. The lower layer is always at rest and infinitely deep. The densities of the upper and lower layers are ρ_1 and ρ_2 respectively. Vertical mixing, vertical viscosity and bottom friction were not included. We model horizontal mixing of momentum using a Laplacian diffusion with uniform eddy diffusivity. The eddy viscosity coefficient (ν) was one of the main parameters of the problem and was varied from 50 m^2/sec to 150 m^2/sec. This range is comparable to some of the values used in modern eddy resolving ocean GCMs. For example, in Stanev (1990) the eddy viscosity coefficient was $\nu = 400$ m^2/sec, while Figueroa and Olson (1994) used $\nu = 50$ m^2/sec for a double gyre GCM. The viscous length scale (which will be defined below) in our model was about 13.6 km for the lowest viscosity coefficient of $\nu = 50$ m^2/sec. The grid resolution in the model is chosen so that this viscous length scale can just be resolved.

At the lateral boundaries, boundary conditions of no normal flow and no slip were used. At the surface a rigid-lid approximation was used and a wind stress imposed. The wind-stress forcing was distributed over the whole active layer depth and acted as a body force. We chose a wind stress of the form $(0, \tau) = (0, \tau_0(x/L_x - 1))$ with a uniform positive curl. In the experiments, τ_0 was fixed: $\tau_0 = 0.5$ dyn/cm^2. The positive sign of the curl corresponds to the cyclonic annual average wind forcing over the Black Sea. In future research, we intend to examine the effects of a time-dependent wind stress, but in this paper the wind stress is steady.

The governing equations, describing a single shallow layer of fluid lying over an infinitely deep layer of denser fluid below and forced with the chosen wind stress, are

$$\begin{aligned}
&\frac{\partial u}{\partial t} + u\frac{\partial u}{\partial x} + v\frac{\partial u}{\partial y} - fv = -g'\frac{\partial h}{\partial x} + \nu\nabla^2 u + \frac{\tau}{\rho_1(h+H)} \\
&\frac{\partial v}{\partial t} + u\frac{\partial v}{\partial x} + v\frac{\partial v}{\partial y} + fu = -g'\frac{\partial h}{\partial y} + \nu\nabla^2 v \qquad (1) \\
&\frac{\partial h}{\partial t} + \frac{\partial}{\partial x}(u(H+h)) + \frac{\partial}{\partial y}(v(H+h)) = 0,
\end{aligned}$$

where h is the deviation of the upper layer depth from H and $g' = g(\rho_2 - \rho_1)/\rho_1$ is the reduced graviational acceleration.

A quasi-geostrophic approximation of the governing equations gives rise to the Equivalent Barotropic (EB) model. The derivation of the corresponding vorticity equation for the EB model can be found in Pedlosky (1987). Although the EB model lacks fast internal gravity waves and is strictly valid only for interface deviations that are small in comparison to the total depth of the active layer (due to the quasi-geostrophic approximation), it still

reproduces Rossby waves, overall basin dynamics, and has found wide use. Given the anticipated sizes of the dynamical changes in the upper layer depth, it would be physically more appropriate to use the shallow water approximation, but quasi-geostrophy gives results qualitatively similar to those of the shallow water model in circulation regimes far from an isopycnal outcropping, which is the case here. Some experiments were made with a shallow water reduced-gravity (1.5-layer) model, for purposes of comparison with the EB model. In those it was found that the maximal interface deviation, corresponding to the strong western recirculation gyre, was about one quarter of the total active layer depth. A great advantage of the quasi-geostrophic models is their computational efficiency because, in the absence of fast gravity waves, one can use longer time steps in the numerical scheme. A computational study of the bifurcation structure of this model then becomes feasible.

The EB model fails to incorporate physical processes such as baroclinic instability. The effect of baroclinic instability on the dynamics of the wind-driven circulation is addressed in a companion study (Berloff and Meacham, 1997a) which uses a two-layer quasi-geostrophic model. The baroclinic model yields bifurcation sequences that differ from those reported in this work, although the general route to chaos is similar to the one found in the EB model and reported here. Through the agency of baroclinic instability, time dependence appears at a lower Reynolds number than in the EB model. However, simple periodic and quasi-periodic motion is seen over a broader range of Reynolds number as the eddies spin up in the lower layer. The flows in the baroclinic model, though low-dimensional, tend to contain a more prominent Rim Current with more energetic meanders.

We chose the upper layer thickness at rest to be $H = 200$ m. The density jump across the interface between the upper and the lower layers was $\rho_2 - \rho_1 = 2.625 \times 10^{-3}$ kg/m^3, yielding a reduced gravity $g' = 2.575 \times 10^{-2}$ m/sec^2. An important parameter of the problem is the Rossby deformation radius, which is $Rd \equiv \sqrt{g'H}/f_0$. The choice of the basin's west-east and south-north sizes, active layer depth and density jump was prompted by the size and hydrology of the Black Sea.

In the potential vorticity/stream function formulation of the EB model (Pedlosky, 1987), we use the following scalings: L_x for the length scale, $(\beta_0 L_x)^{-1}$ for the time scale, U for the velocity scale and τ_0 for the wind-stress scale. We specify the velocity scale from the Sverdrup balance: $U = \tau_0/\rho H L_x \beta_0$ and introduce the following dimensional length scales in addition to Rd, L_x and L_y:

$$\delta_I = \sqrt{\frac{U}{\beta_0}}; \qquad \delta_M = \sqrt[3]{\frac{\nu}{\beta_0}}.$$

Here δ_I is an inertial length scale and δ_M is a viscous length scale or Munk scale (Pedlosky, 1987). The nondimensional parameters of the problem now are

$$\delta = \frac{L_x}{L_y}; \qquad \epsilon = \left(\frac{\delta_I}{L_x}\right)^2; \qquad \mu = \left(\frac{\delta_M}{L_x}\right)^3; \qquad S = \left(\frac{L_x}{Rd}\right)^2.$$

Here δ is an aspect ratio of the rectangular basin, ϵ is a squared ratio of the inertial length scale to L_x, μ is a cubed ratio of the Munk scale to L_x, and S is the square of the ratio of the zonal geometrical length scale to the Rossby deformation radius. The limit $S = 0$ yields the purely barotropic problem. Using the nondimensional parameters, we can write the potential-vorticity equation in the following nondimensional form

$$\frac{\partial}{\partial t}(\nabla^2\psi - S\psi) + \epsilon J(\psi, \nabla^2\psi) + \frac{\partial\psi}{\partial x} = \nabla \times \tau + \mu\nabla^4\psi. \tag{2}$$

The parameter δ does not enter (2) directly but arises in the specification of the boundary conditions.

The numerical model solves (2) in dimensional form. The horizontal resolution in the model was 6.25 km on a 129×65 grid. We solved the potential vorticity equation using second order spatial finite differences and an explicit leapfrog scheme for time stepping. The nonlinear term was discretized following Arakawa (1966) and does not artificially generate energy.

The normal component of velocity at the boundary of the basin is zero, yielding the boundary condition:

$$\psi|_C = \Gamma_0(t), \tag{3}$$

where $\Gamma_0(t)$ depends upon time only and C is the boundary around the basin. We use the no-slip condition on the velocity along the boundaries of the basin,

$$\frac{\partial\psi}{\partial n}|_C = 0, \tag{4}$$

where $\mathbf{n}$ is the normal to C. Another constraint imposed upon the stream function is

$$\frac{\partial}{\partial t}\int\int_A \psi(x, y)\, dx\, dy = 0, \tag{5}$$

which is the conservation of mass law for fluid in a basin of area A.

The numerical procedure included time-stepping equation (2) for the potential vorticity, $\zeta \equiv \nabla^2\psi - S\psi$, with boundary conditions (3) and (4), and then solving the elliptical Helmholtz problem

$$(\nabla^2 - S)\psi = \zeta \tag{6}$$

for ψ with the mass conservation constraint (5). The Helmholtz problem was solved using a FACR method (Hockney, 1970). We checked the effects of truncation error by making several runs in which the grid resolution was doubled and the time step was halved. The results are discussed in Section 5.

The system we investigate is a discrete dissipative forced dynamical system with a

dimension equal to the number of nodes in the basin multiplied by the number of variables at each node. When we solve the present EB problem (which has only one variable ψ), this dimension, which we'll refer to as p, is more than 8000. Each state of the system, i.e. potential vorticity distribution at the nodes of the grid, corresponds to a point in this p-dimensional phase space, and as the system evolves, this phase point traces out a trajectory in this space. Thus we work with an autonomous discrete dynamical system with states $\mathbf{x}(t)$, that are governed by the set of equations

$$\dot{\mathbf{x}} = \mathbf{F}(\mathbf{x}(t, \mathbf{x}(0)); \mathbf{a}) \tag{7}$$

where $\mathbf{x}(0)$ is the initial state of the system and $\mathbf{a}$ is a set of control parameters. We varied two control parameters—the horizontal eddy viscosity coefficient ν and the Rossby deformation radius *Rd.* Thus, in a first set of experiments, we changed the nondimensional parameter μ by varying the viscosity and keeping all other nondimensional parameters fixed; and in a second set of experiments we changed the nondimensional parameter S by varying the deformation radius *Rd.* We have not studied the effects of δ and ϵ variations.

3. Methodology

First, we integrated the model forward in time until it converged asymptotically to some attractor in the full phase space. The time required for the system to asymptote was typically in the range 10^4–10^5 days, depending upon the rate of convergence. To decide whether the trajectory converged or not and to characterize the nature of the attractor, we used a combination of analysis techniques. We describe these briefly here.

a. Projections into reduced phase spaces. To construct a low-dimensional projection of the full p-dimensional phase space, we used the *method of delay coordinates,* (Packard *et al.,* 1980; Takens, 1981). We recorded a time series of the dimensionless total energy $\int_D E(t)$, $= \int_D |\nabla\psi|^2/2 + S\psi^2/2$, where $\int_D$ denotes integration over the basin. To construct a projection of the system trajectory in a reduced phase space, we defined a time-dependent n-dimensional vector $\mathbf{x}(t; \vartheta) \equiv (x_1, x_2, \ldots, x_n)$, where ϑ is a fixed positive time delay and

$$x_j = E(t - j\vartheta), \qquad j = 0, 1, \ldots, n - 1.$$

The best choice of ϑ is one such that x_j is not closely correlated with x_{j-1}, which would be the case if ϑ is too small; and not completely uncorrelated, as would happen if ϑ were too large. Sensible choices of ϑ include the time to the first zero-crossing of the autocorrelation function or the time to the first minimum of the mutual information function (Fraser and Swinney, 1986). The exact choice of ϑ is not critical; varying ϑ over a modest range around say the quarter period of the fastest dominant frequency merely distorts the shape of the attractor but does not hide its topology which is the fundamental property of interest (see Brandstater and Swinney, 1987). For the present problem, we fixed $\vartheta = 30$ days. Using $n = 3$, the trajectory can be visualized by plotting the trajectory in the reduced space (x_0, x_1, x_2).

We use the delay technique to identify different attractors with respect to various ν and initial conditions. Ideally, the choice of projection dimension n of the p-dimensional phase space should depend upon the dimension of the dominant attractor. According to one of Whitney's *embedding theorems* (Whitney, 1936; Takens, 1981), a smooth compact manifold of dimension m in p-dimensional space may be represented without self-intersection in a subspace with dimension $n = 2m + 1$. However, attractors are typically recognizable in projection spaces of lower dimension than $2m + 1$, though they often exhibit self-intersection.

b. Power spectra. Another useful approach for determining the characteristic frequencies of motion on an attractor, and for distinguishing between quasi-periodic and chaotic motion, is to compute the Fourier power spectrum of a time series. We computed power spectra of time series of the total energy integrated over the basin.

c. Poincaré sections. Poincaré sections through low-dimensional attractors in the delay space are also useful for distinguishing different types of attractor. We constructed these by picking a fixed plane through an attractor and plotting the linearly interpolated intersection of a trajectory with the plane each time a trajectory passes through the plane in one direction.

d. Unstable steady states. An unstable solution cannot be detected by a simple time-stepping approach; therefore, in order to find unstable steady solutions, we used the following techniques. One of them was to reduce the deformation radius in the upper layer artificially and by that trick to stabilize the solution. Integration in time of the stabilized equations of motion yields a steady solution that would be unstable at the original *Rd*. In the steady state limit the time derivative vanishes and the artificial *Rd* reduction doesn't matter. In fact, all steady states of the EB model are steady states of a barotropic model with a layer depth equal to that of the active layer of the EB model. In general though, the stability properties of the steady states in the two types of models are different.

Another approach was to compute a small amplitude limit cycle and time-average it over one period of oscillation. We used the time-averaged state as a new initial condition (the time-averaged state is close to the unstable steady state, but does not coincide with it) and integrated forward in time until the trajectory began to spiral out in the direction of the stable initial limit cycle. This spiral trajectory was time-averaged again over one cycle and the process was iterated. This procedure converges only if the initial limit cycle is close enough to the unstable steady state. Empirically, this appeared to be the case for small amplitude limit cycles in the vicinity of the primary bifurcation threshold. The amplitudes of the successive spirals, computed in this iterative procedure, provided a measure of the proximity to the unstable steady state and allowed us to decide when to terminate the iterations.

e. Eigenmodes. For some of the unstable steady states that were close to the marginal stability threshold, we searched for an unstable linear eigenmode using the following procedure. We used a linear version of the evolution model. The unstable steady state was used as the basic state (about which the model was linearized), and the model was initialized with a small perturbation. The linear model was integrated forward in time for several eigenperiods. The eigenperiods were estimated from the periods of the nearby stable limit cycles. At the end of the integration, the evolved perturbation was rescaled, reducing its amplitude back to a small initial level. The integration forward in time was then repeated with the rescaled field as the new perturbation. After several iterations we were left with something close to the most unstable linear eigenmode. A delay coordinate projection of the final iteration of this procedure looks like an exponential spiral, diverging from the unstable fixed point. From the spiral, we can extract the growth rate and frequency of the unstable eigenmode by a least squares fit to a complex exponential.

f. Fractal dimension. One of the relevant quantities characterizing an attractor of a dynamical system is its dimension. A variety of different definitions of dimension is discussed in Farmer *et al.* (1983). Motion on attractors with noninteger dimension often exhibits sensitive dependence on initial conditions and can be regarded as a form of chaotic motion. Estimating dimension is an appropriate way to describe a chaotic system and distinguish it from a stochastic one. In the latter case, a trajectory is not attracted to any low-dimensional subset, and instead would occupy a large-dimensional part of the whole p-dimensional phase space. Calculating the power spectrum fails to clearly distinguish between these two cases, since it yields broad band structure for both (although, given enough resolution, the way in which the two types of spectra fall off at high frequency can be revealing).

Let us define the information dimension D of an attracting set in p-dimensional phase space. We imagine covering the attractor with small p-dimensional hypercubes of side ϵ, and set $N(\epsilon)$ equal to the minimum number of cubes of size ϵ needed to cover the attractor. Then,

$$D = \lim_{\epsilon \to 0} \frac{I(\epsilon)}{\log\left(\frac{1}{\epsilon}\right)},$$

where

$$I(\epsilon) = \sum_{i=1}^{N(\epsilon)} P_i \log \frac{1}{P_i}$$

and P_i is the probability that a phase point on a typical trajectory on the attractor is contained within the ith cube. To estimate the information dimension of a chaotic attractor we used the *nearest neighbor algorithm* (Badii and Politi, 1985; Kostelich and Swinney,

1987). The basic idea of the method is the following. First, we compute a time series, corresponding to a trajectory on or very close to an attractor. Let the total number of points in the series be N. We choose M reference points $\mathbf{x}(m)$ $(1 \leq m \leq M)$ and for each of them choose a random set of k_1 other points. We compute distances $\delta(m, k_1)$ between $\mathbf{x}(m)$ and its nearest neighbor $\mathbf{y}(m)$ from the k_1 points. We repeat the procedure for increasing values of k_j, such that $k_{j-1} < k_j \ll N - 1$. The resulting function $\delta(m, k)$ is recorded. The overall procedure is repeated for all M reference points. The underlying idea of the method is that

$$\langle \delta(k) \rangle \stackrel{\text{def}}{=} \sum_{m=1}^{M} \frac{\delta(m, k)}{M} \sim k^{-1/D}, \qquad k \to \infty, \quad k \ll N.$$

From this asymptotic scaling in the limit of large M we can estimate the dimension D. An average time series length N for our problem was about 2×10^5. The number M of reference points we used was 4000. The method was implemented using the software of Kostelich (1990).

4. Results. The bifurcation sequences

a. Viscosity coefficient as the control parameter. Keeping a fixed deformation radius, $Rd = 24.4$ km, we have explored the viscosity coefficient range $54 \leq \nu \leq 150$ m^2/sec and identified a sequence of attractors in this range. For $\nu > 104$ m^2/sec, the solutions are stationary and stable. In the p-dimensional phase space of the full numerical model, each solution corresponds to a stable fixed point with a specific value of energy. A sequence of steady solutions with different values of $\nu = 1000, 500, 300, 200, 105, 60$ m^2/sec is shown as the stream function plots in Figure 2a (the last picture corresponds to a steady unstable solution and we'll discuss it later). One can see how a steady, meandering return flow and a set of strong recirculations form in the southern part of the basin. Scatterplots of ζ versus ψ, for the same values of ν, respectively, as on the previous figure, are shown in Figure 2b. In this figure, only points with $\psi < 40$ are used. The points corresponding to the recirculations are scattered along the straight lines. This tendency indicates an approximately linear functional relationship between ζ and ψ within the recirculations. From Figure 2b, one can see that the values of $d\psi/d\zeta$ within each gyre are slightly different for different steady solutions. The last two pictures, corresponding to $\nu = 105$ and 60 m^2/sec, indicate that the several gyres within a given steady state have approximately the same value of $d\psi/d\zeta$. The negative slopes of the scatterplots, together with the fact that the scale of the gyres are considerably larger than the deformation radius, are consistent with the idea that the vorticity balance within the gyres is maintained by down-gradient eddy transport as suggested by Marshall and Nurser (1986). We conclude that the tendency toward a linear functional relation within the gyres seems to be robust for the problem at hand. This suggests that the recirculation in each gyre is mainly dominated by inertia.

The picture that corresponds to the fixed point with $\nu = 105$ m^2/sec (see Fig. 2a) shows a steady circulation at a value of ν very close to the primary bifurcation. This solution has

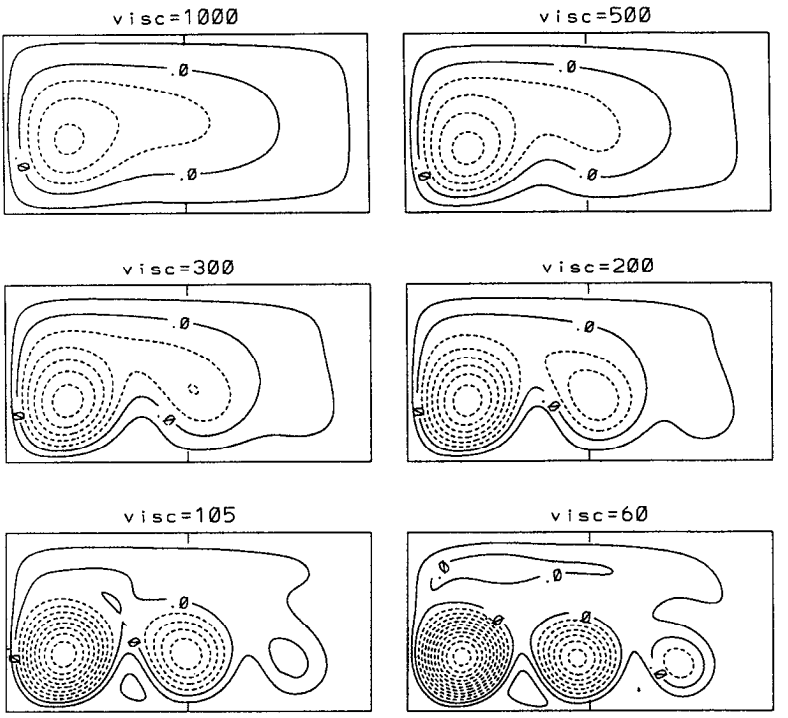

Figure 2. (a) Stream function plots of six different steady solutions at the values of ν = 1000, 500, 300, 200, 105, 60 m^2/sec. Note how the recirculation gyres develop as ν decreases. The last picture at ν = 60 m^2/sec corresponds to an unstable fixed point. Contour interval (CI) = 40 (nondimensional units). (b) Scatterplots of ψ versus ζ for the six steady solutions in Figure 2a. The samples were taken within the contour ψ = 40. (Units for ψ and ζ are dimensionless.)

three distinctive cyclonic inertial gyres of unequal sizes. The strength of the gyres, in terms of absolute velocities and sizes, decreases eastward. Values of the absolute velocity are shown in Figure 3; and one can see that the velocity is maximal in bands that correspond to the sides of the first meander between the western and central gyres and the part of the western intensification where an inflow from the interior merges with fluid circulating in the western gyre.

Below ν = 104 m^2/sec, the branch of fixed points continues but now the points are unstable and represent a family of unstable steady solutions. To compute the unstable solutions, we followed the techniques described in Section 3. The full energies of both stable and unstable fixed points are shown in Figure 4 as a function of ν. The main branch for $\nu > 104$ m^2/sec consists of stable fixed points; for $\nu < 104$ m^2/sec, the lower branch corresponds to unstable fixed points while the upper branch of mean energies in Figure 4 corresponds to time-dependent solutions which will be discussed later. The steady unstable solution at ν = 60 m^2/sec is shown on the last panel of Figure 2a.

For the chosen value of *Rd,* 24.4 km, the threshold between the stable and unstable fixed

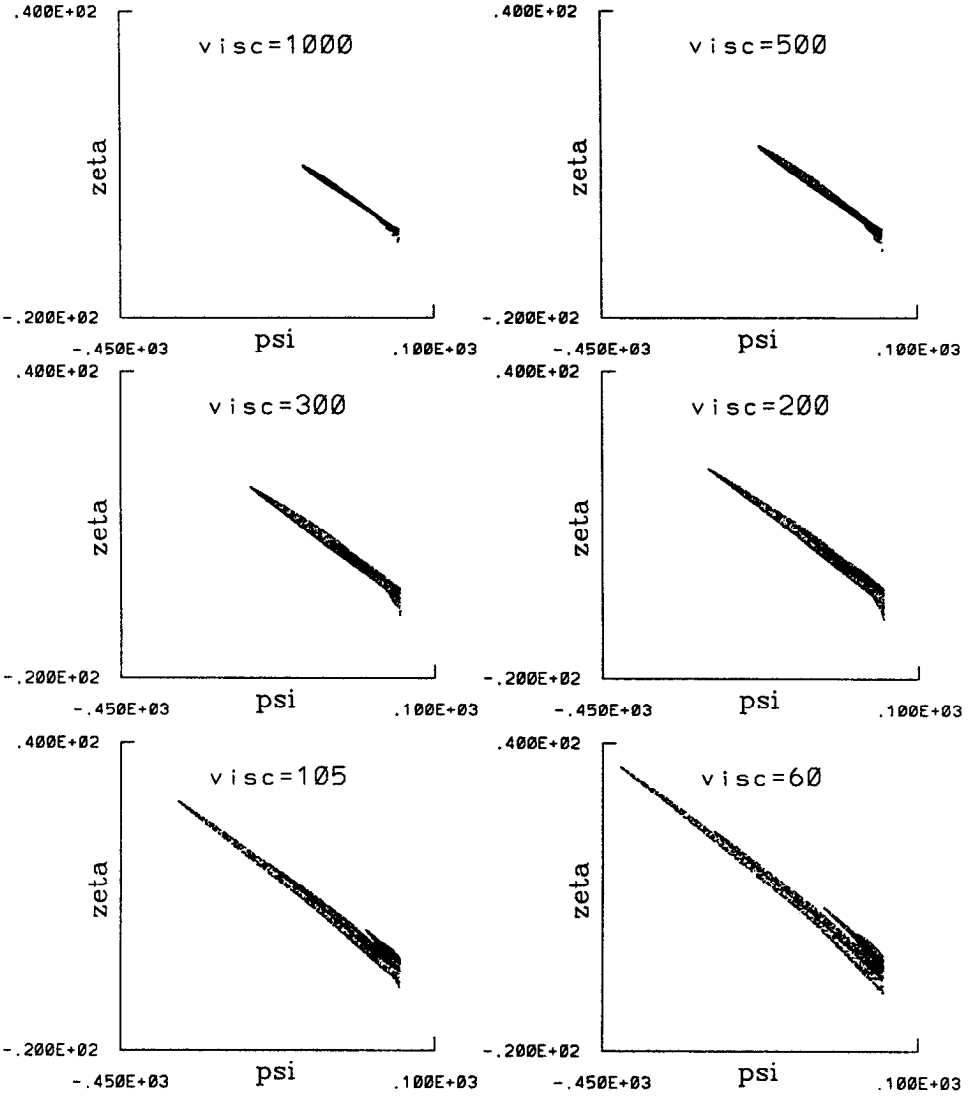

Figure 2 (Continued)

points in the model lies between 103 and 104 m^2/sec values of ν. Numerical experiments made for different values of *Rd* suggest that the stability threshold (or the primary bifurcation as we'll refer to it) occurs at lower values of ν if *Rd* is decreased. In other words, a longer deformation radius has, in general, a destabilizing effect on the circulation model.

Destabilization of the family of fixed points is associated with the appearance of stable limit cycles (see the phase space projection of the limit cycle for $\nu = 100$ m^2/sec in

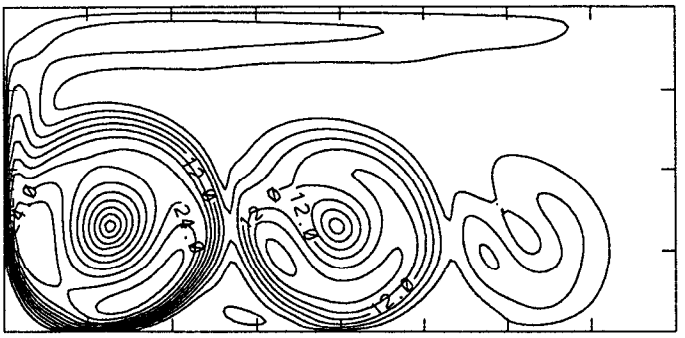

Figure 3. Values of the absolute velocity at $\nu = 105$ m^2/sec. The contour interval is 3.0 cm/s.

Figure 5). We identified the first (the primary) bifurcation as a supercritical Hopf bifurcation, associated with the onset of oscillatory instability of a steady solution and the appearance of a stable limit cycle. For this type of bifurcation, the real part of the pair of complex conjugate eigenvalues of the two least unstable linear eigenmodes becomes positive and the modes begin to grow in amplitude. In Figure 6, we show the behavior of the limit cycle amplitudes in the vicinity of the Hopf bifurcation threshold. The amplitude of the limit cycles shown in this figure scales as $.22\sqrt{\nu - 103.5}$ close to the threshold.

In phase space, a trajectory that starts close to the unstable fixed point spirals outward until it converges to a limit cycle. The limit cycle computed for $\nu = 103$ m^2/sec, which is slightly below the stability threshold, has a period of 113 days. The periods of the most unstable growing linear eigenmode computed for the unstable fixed point at $\nu =$

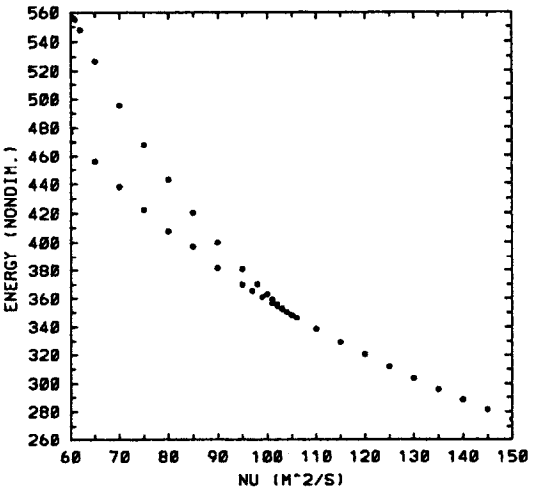

Figure 4. Energies of the stable/unstable fixed points and mean energies of the limit cycles versus ν. For the values of ν below the critical point associated with the primary bifurcation, approximately $\nu = 103.5$, the lower branch corresponds to unstable fixed points and the upper branch to limit cycles. For the values of ν above the critical point there are only stable fixed points.

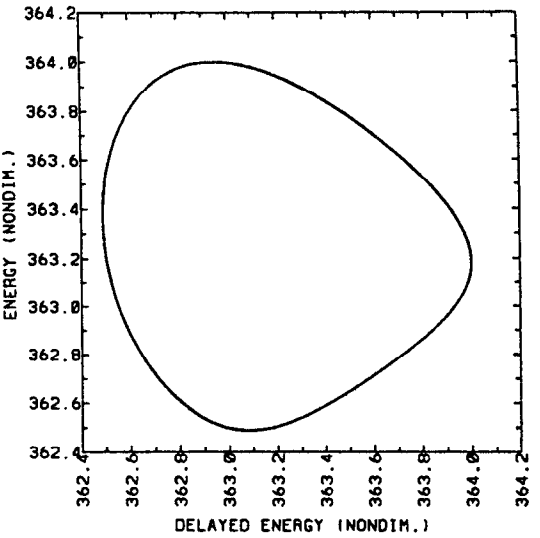

Figure 5. The delay coordinate phase space projection of the limit cycle at $\nu = 100$ m^2/sec.

103 m^2/sec and of the least stable decaying linear eigenmode, computed for the stable fixed point at $\nu = 105$ m^2/sec, are both approximately 112 days.

A limit cycle in phase space corresponds to oscillatory (periodic) behavior of the circulation in the basin. In Figure 7a, we show the spatial and temporal structure of the limit cycle oscillation for $\nu = 75$ m^2/sec. For this purpose, we subtracted the steady unstable solution at $\nu = 75$ m^2/sec from the time-dependent stream function on the limit

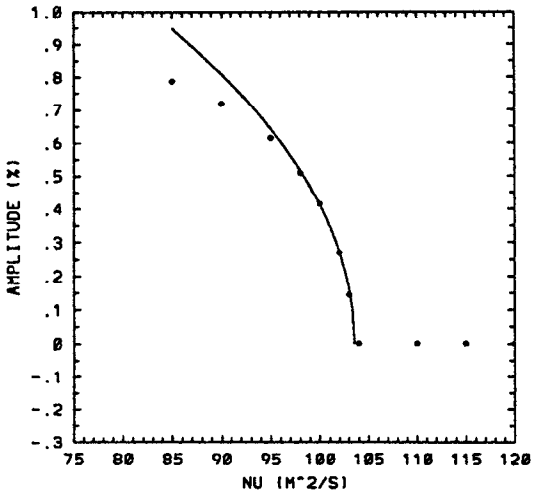

Figure 6. The oscillation amplitudes (circles) as a percentage of mean amplitude versus ν. In the vicinity of the critical point the amplitude scales as $0.22\sqrt{\nu - 103.5}$ (solid curve).

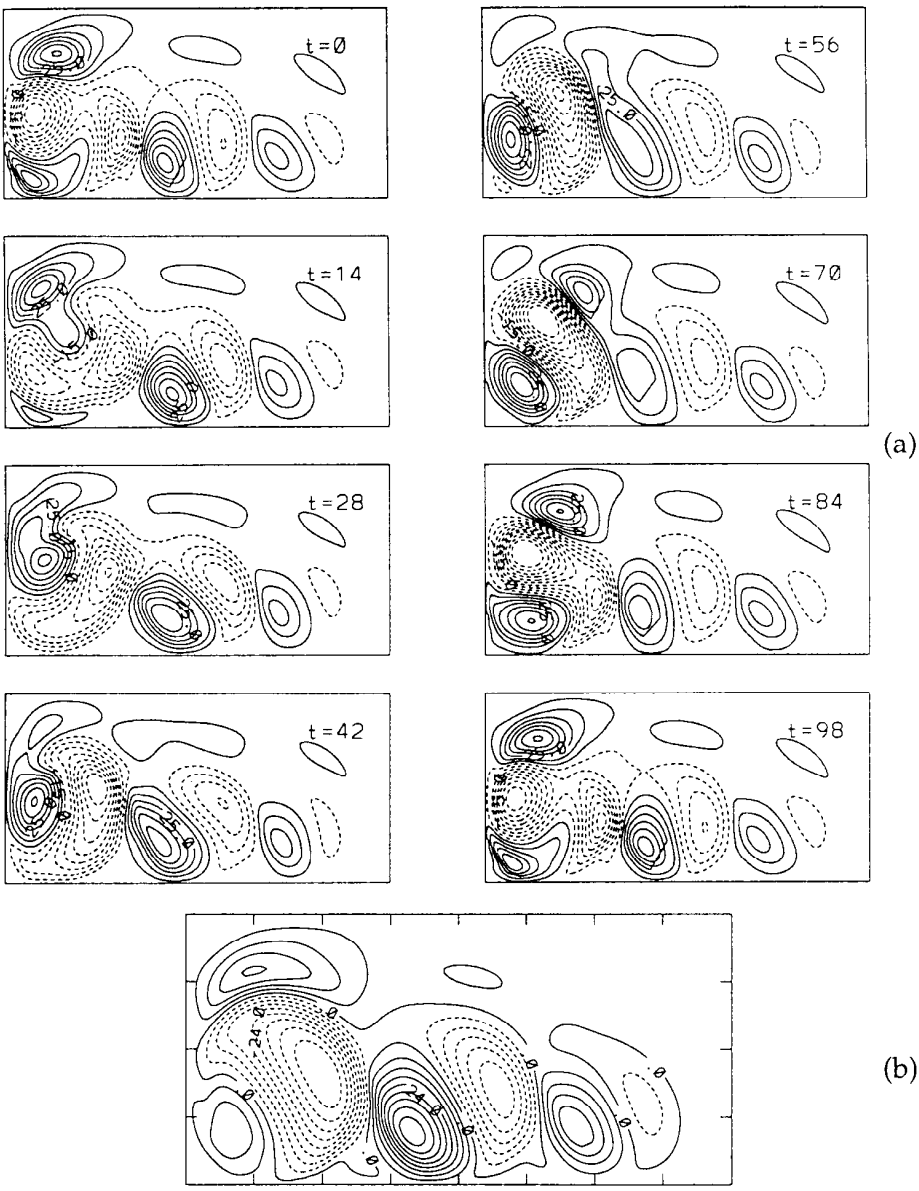

Figure 7. The behavior of the circulation over the limit cycle at $\nu = 75$ m^2/sec. The oscillations of the total energy in the limit cycle have an amplitude of approximately 3.5% of the mean. Time t is measured in days. (a) The unstable steady state stream function subtracted from the time-dependent stream function corresponding to the limit cycle. CI = 10; (b) The difference between stream functions of the time-averaged and unstable steady states. CI = 6; (c) The time-averaged stream function subtracted from the time-dependent one. CI = 10.

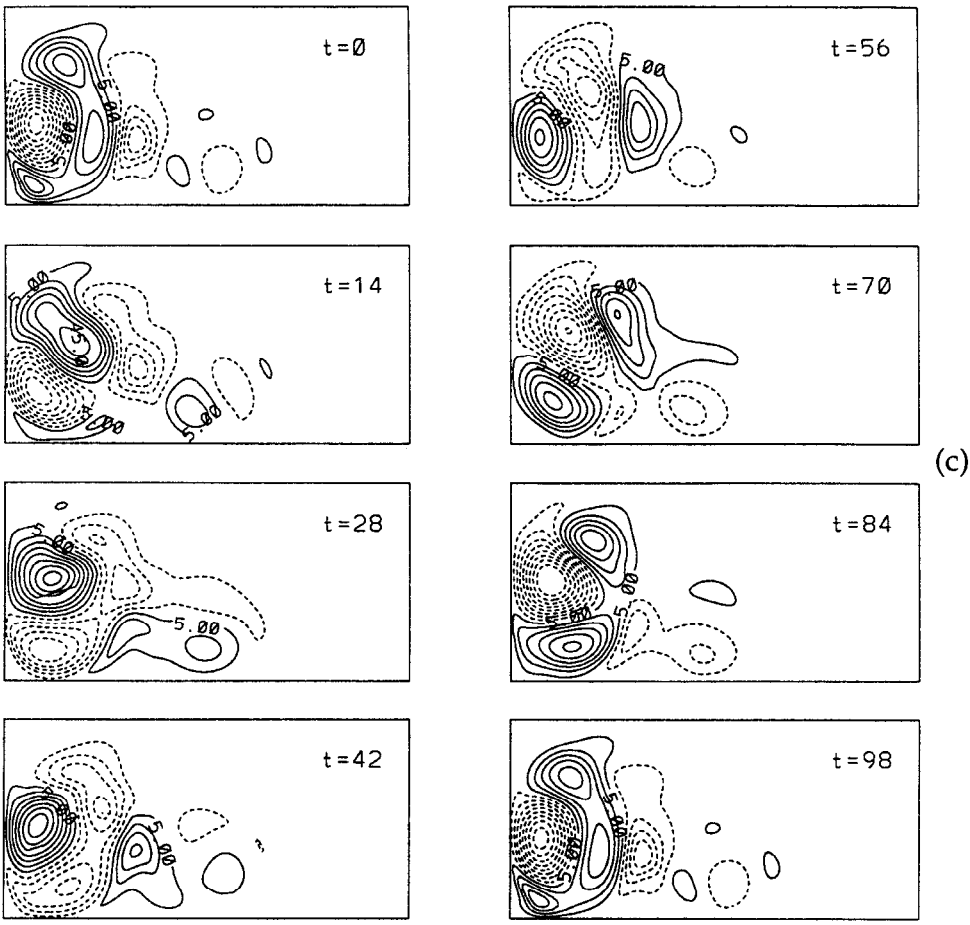

(c)

Figure 7. (Continued)

cycle. The perturbation stream function

$$\psi_1'(x, y, t) = \psi(x, y, t) - \psi_{\text{unst}}(x, y),$$

is then shown in Figure 7a. In Figure 7b we show the difference between the time-averaged stream function $\langle\psi(x, y, t)\rangle = 1/T \int_{t_0}^{t_0+T} \psi(x, y, t)\, dt$, where T is one period of the limit cycle, and the stream function of the unstable steady state $\nu = 75$ m^2/sec. The pattern from this figure is consistent with a slight displacement of the recirculation gyres to the east. The difference between the time-dependent stream function on the limit cycle and the time-averaged stream function is

$$\psi_2'(x, y, t) = \psi(x, y, t) - \langle\psi(x, y, t)\rangle.$$

We show $\psi'_2(x, y, t)$ in Figure 7c. Looking at the spatial and temporal structure of $\psi'_2(x, y, t)$, we see that the oscillation is mostly active in the western part of the basin including the western boundary intensification and the western recirculation gyre. Two important features of the oscillation may be observed from Figure 7c: first, $\psi'_2(x, y, t)$ is localized in the western part of the basin; second, it contains a series of eddies, which are cyclonically advected around the western recirculation gyre. The oscillations of the total energy in the limit cycle at $\nu = 75$ m^2/sec are 3.5%; and the absolute perturbation velocity $U' = |\nabla\psi'_2|$ reaches a maximum of 0.15 m/sec during the limit cycle.

We traced the branch of stable limit cycles down to $\nu = 60.5$ m^2/sec. The values of the mean energy of the periodic attractors versus ν are shown by the upper branch of points in Figure 4. We computed the mean energy as an arithmetical mean between the highest and the lowest values of energy achieved on the attractor. The mean energy values of the limit cycles are bigger than those associated with the unstable steady states at the same values of ν. The period of the limit cycles decreases gradually down to 90 days for the last limit cycle at $\nu = 60.5$ m^2/sec (see frequencies versus ν in Fig. 8b). The variation of the amplitudes (we define the amplitude as the largest deviation of the total energy from the mean) of the periodic solutions with respect to ν is shown on the bifurcation diagram (Fig. 8a). The diagram shows that, from the primary to the secondary bifurcation, at which the limit cycle solution loses stability (between $\nu = 60.3$ m^2/sec and $\nu = 60.5$ m^2/sec), the amplitude changes in a smooth fashion.

For the slightly supercritical value of $\nu = 100$ m^2/sec, we filtered out numerically the most unstable growing eigenmode, following the method described in Section 3. The spatial structure and the time-dependent behavior of the linear eigenmode are presented in Figure 9. The sequence of snapshots corresponds to one oscillation, or, more accurately, to one period of the spiraling phase space trajectory around the unstable fixed point. During this revolution, the eigenmode grows in amplitude by 11.7%. Further integration in time shows that the trajectory finally converges to a limit cycle. In Figure 7c one can see that the spatial structure and the time-dependent behavior of the limit cycle at $\nu = 75$ m^2/sec look similar to those of the linear eigenmode. At small oscillation amplitudes, which is the case here, it appears that nonlinear oscillations in the limit cycles are just the most unstable eigenmodes modified slightly by nonlinearity.

One approach that proved useful for exploring the nature of the primary instability of the circulation was to look at the energetics of the most unstable linear eigenmode of the steady unstable circulation. Any instability must be a horizontal shear instability but there are several regions of localized shears within the flow that are potential sites of instability. After the most unstable linear eigenmode was isolated, we computed the associated eddy-mean energy conversion term

$$P = -\epsilon\Psi\langle\psi'_x\nabla^2\psi'_y - \psi'_y\nabla^2\psi'_x\rangle.$$

Here Ψ is the slowly varying mean stream function obtained by averaging over one cycle of the unstable eigenmode and ψ' is the rapidly varying part of the stream function, $\psi' =$

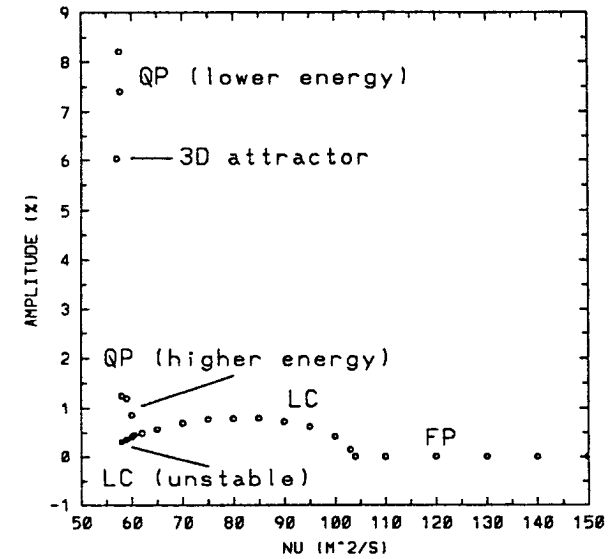

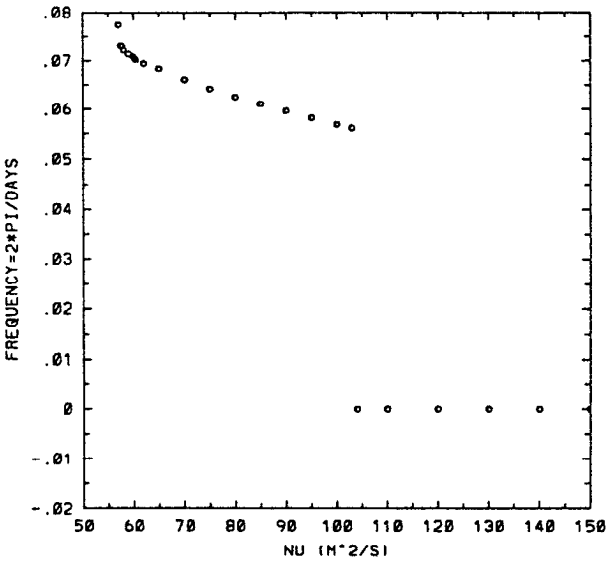

Figure 8. (a) Bifurcation diagram. The oscillation amplitude as a percentage of mean amplitude versus ν. FP—fixed points; LC—limit cycles (unstable limit cycles are shown with filled circles); QP—quasi-periodic motion on toroidal attractors. The amplitude of the chaotic attractor at ν = 56 m^2/sec is about 14% and it is not shown on this diagram. (b) Bifurcation diagram. The basic frequency of the oscillations versus ν.

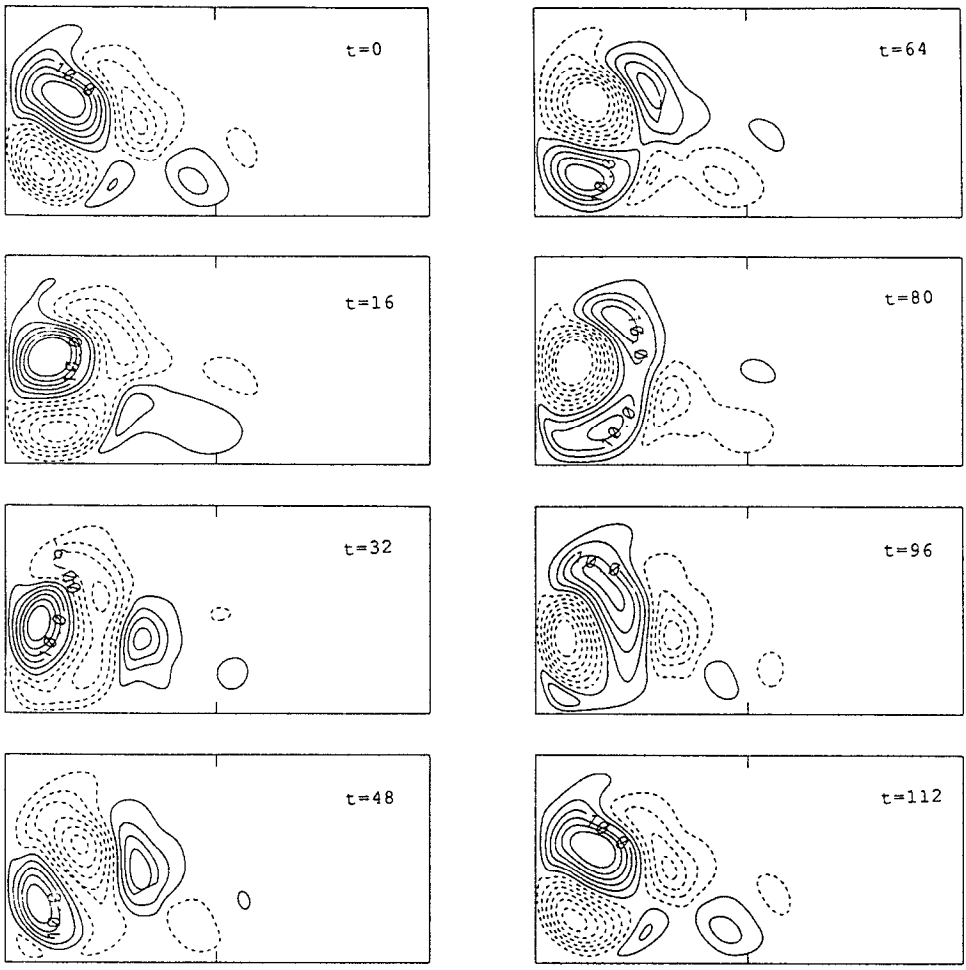

Figure 9. Time-dependent behavior of the stream function of the most unstable eigenmode at ν = 100 m^2/sec over one eigenperiod. Note, that the eigenmode is trapped in the western part of the basin. Time t is measured in days. CI = 4.

$\psi - \Psi$. When the area integral of P is positive, perturbations grow, gaining energy from the mean state. When the integral of P is negative, perturbations decay, transferring energy to the mean flow. The spatial structure of P for the most unstable eigenmode at Rd = 24.4 km and ν = 100 m^2/sec is shown in Figure 10. The dominant maximum and minimum of P are concentrated near the confluence of the western boundary current and the recirculating flow in the western gyre. There are also two smaller extrema of P in the southwest corner of the domain, one against the western boundary and one against the southern boundary. Lastly there is a weak maximum to the east of the standing meander crest that lies just to the east of the western recirculation. It seems that the instability is a complex instability of

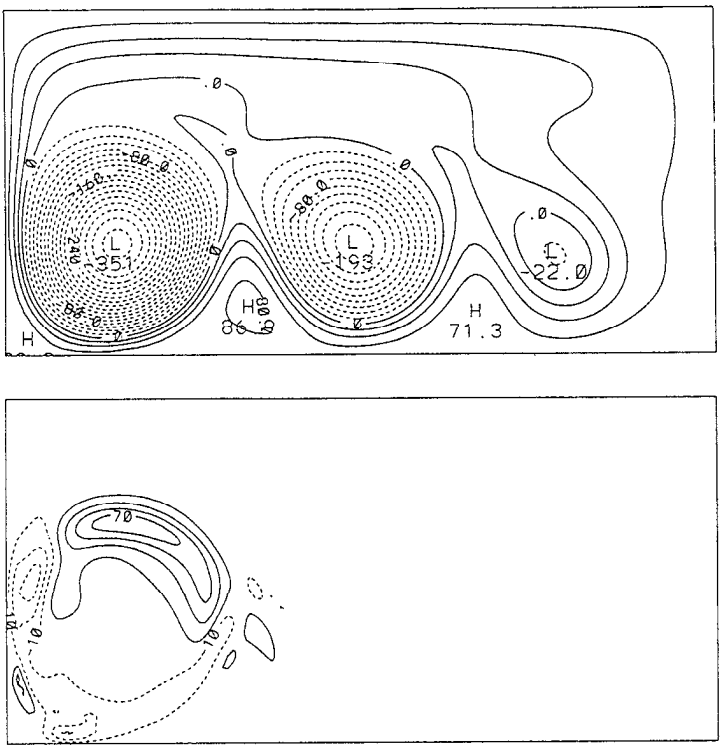

Figure 10. The spatial distribution of (a) the mean stream function and (b) the energy conversion term, P, at $\nu = 100$ m^2/sec and $Rd = 24.4$ km. Dimensionless CI = 20 in each.

the part of the flow that consists of the western boundary intensification and the western gyre with some coupling to the meander between the western and the central gyres.

Berloff and Meacham (1997b) studied the primary equivalent-barotropic instability in basins with different aspect ratios δ and showed that, in addition to the complex instability found in our case, there are two possible mechanisms of flow instability. One kind of instability is localized in the western boundary current only. It is analogous to the barotropic western boundary current instability studied by Ierley and Young (1991). The second kind of instability is associated with the meander between the western and the central gyres.

As we saw in Figure 8a, the amplitude of the limit cycle changes smoothly as ν is reduced until an oscillatory instability of the limit cycle occurs between $\nu = 60.3$ m^2/s and $\nu = 60.5$ m^2/s. A toroidal attractor was computed at $\nu = 60.3$ m^2/sec (see Fig. 11a,b which show a phase space projection of a trajectory on the attractor and the associated Poincaré section). The typical behavior of a trajectory trapped to such an attractor is either quasi-periodic motion with two frequencies, the ratio of which is not a rational number or, if the frequency ratio is sufficiently close to rational that phase locking may occur, a limit cycle embedded on the torus. Poincaré sections of quasi-periodic or long period limit cycle

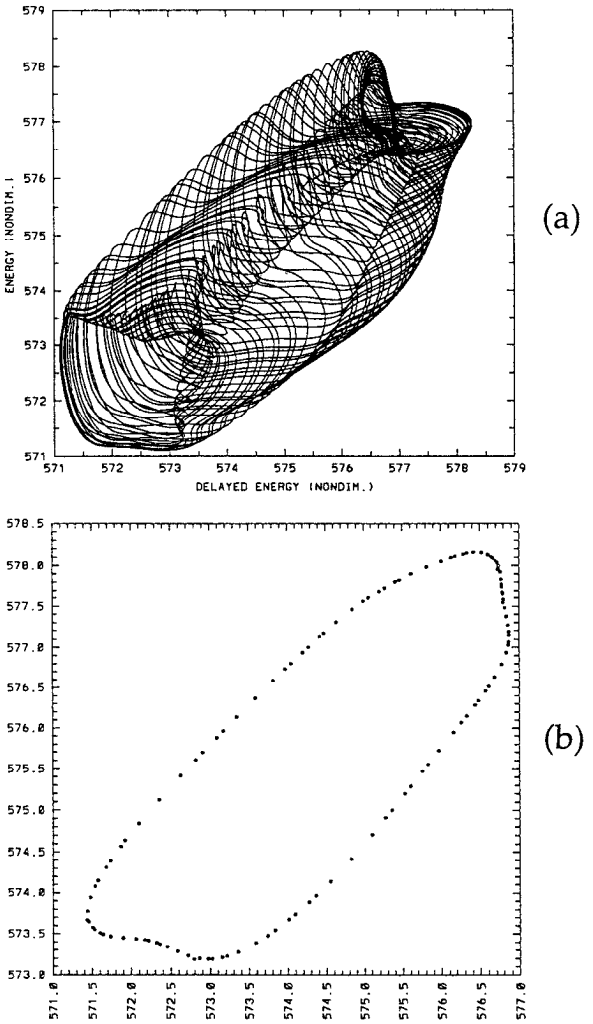

Figure 11. (a) A delay coordinate phase space projection of the trajectory on the toroidal attractor at $\nu = 58$ m^2/sec; (b) Poincaré section of the trajectory on the toroidal attractor at $\nu = 58$ m^2/sec.

trajectories on a toroidal attractor consist of points lying on a curve (or set of curves). This helps to distinguish this class of attractors from limit cycles and chaotic attractors. In what follows, we are not able to distinguish between quasi-periodic and very long period limit cycles on a torus, therefore we will somewhat inaccurately refer to both of these motions as "quasi-periodic."

The limit cycle becomes unstable for ν just above 60.3 m^2/sec. The family of limit cycles probably continues as a family of unstable periodic solutions for decreasing viscosity. It would be interesting to find an unstable oscillatory solution, corresponding to an unstable limit cycle, but this is beyond the scope of this paper, and we concentrate here mainly on

the stable attractors (with an exception made for fixed points and some weakly unstable limit cycles). The second bifurcation (from limit cycle to torus) also appears to be a Hopf bifurcation (Drazin, 1992). In principle, the stability of the limit cycle could be analyzed with Floquet theory. The new frequency arising at the bifurcation and the growth rate associated with the instability could be estimated from careful study of Poincaré sections, but with our present model this is fairly difficult and we have not attempted it.

The family of stable toroidal attractors continues down to $\nu = 58$ m^2/sec. Quasi-periodic motion on the torus has two frequencies associated with it and, in our case, one frequency, which we'll refer to as the basic frequency, is a continuation of the original limit cycle frequency. The second period, associated with winding around the torus, is about 420 days. Figure 12 shows a power spectrum for the quasi-periodic trajectory on the toroidal attractor, corresponding to $\nu = 59$ m^2/sec. The dominant spikes correspond to periods of about 88 and 420 days for the basic and the second frequencies respectively.

For 57.7 m^2/sec $< \nu < 58$ m^2/sec we observed another bifurcation. The toroidal attractor, which existed at the higher value of viscosity ($\nu = 58$ m^2/sec), becomes weakly unstable at $\nu = 57.7$ m^2/sec; the trajectory leaves it and is attracted to a different torus with a significantly lower energy and different geometrical characteristics. In Figure 13, we superimposed two Poincaré sections. Each section corresponds to a quasi-periodic trajectory winding around a torus, and both sections were computed using the same plane through the three dimensional delay coordinate phase space projection. The trajectory winding around the higher energy torus was computed for $\nu = 58$ m^2/sec and the trajectory around the lower energy torus for $\nu = 57.7$ m^2/sec. The higher energy torus most probably continues to exist as an invariant set for $\nu \leq 57.7$ m^2/sec, but is unstable. It is not clear whether these two tori belong to the same or different families of time-dependent solutions. Since the techniques we are using are not able to locate unstable periodic and unstable toroidal solutions, we cannot resolve this question fully. However, a comparison of the structure of the attractors is quite helpful.

After computing the lower energy attractor at $\nu = 57.7$ m^2/sec, we increased the value of viscosity to $\nu = 58$ m^2/sec and used a point on the trajectory belonging to the lower energy attractor as an initial condition for the model. Integrating in time, we observed that the trajectory returns to the higher energy toroidal attractor. The return to the higher energy torus consists of two stages. During the first stage the trajectory leaves the lower energy torus and collapses to a limit cycle. This stage took about 10^3 days. The limit cycle is weakly unstable. The trajectory diverges from it and is attracted to the higher energy torus on a rather long time scale of $O(10^6)$ days. This is the second stage. The extremely weak instability of the limit cycle lets us continue this branch of unstable limit cycles to higher values of ν. We were able to locate the unstable limit cycles to a good approximation. We computed the unstable limit cycles at $\nu = 58, 59, 60, 60.5$ m^2/sec. In the last run the limit cycle was stable and coincided with the stable limit cycle obtained previously at this viscosity value by continuing more viscous limit cycles to lower ν. The unstable continuation of the stable limit cycle branch is shown in Figure 8a. The periods of the

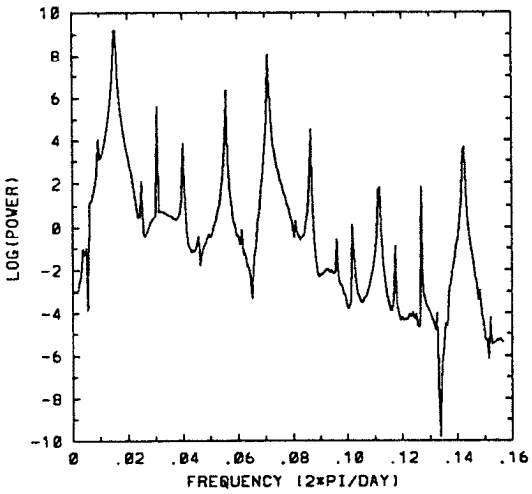

Figure 12. Power spectrum of the time series corresponding to the trajectory on the toroidal attractor at $\nu = 59$ m^2/sec. Note two dominant frequencies 0.015 and 0.071 rad/day (periods are 420 and 88.5 days respectively). The smaller spikes are due to nonlinear interaction between the dominant harmonics.

unstable limit cycles are close to the basic periods of the higher energy toroidal attractors at the same ν values. When we tried to compute the unstable limit cycle at $\nu = 57.7$ m^2/sec using a point on the limit cycle at $\nu = 58$ m^2/sec as an initial condition, the trajectory converged to the lower energy torus.

A possible explanation of the bifurcation from the weakly unstable limit cycle to the torus might be the following. At some value of the viscosity coefficient ν_{1cr} lying between 60.3 m^2/sec and 60.5 m^2/sec, a pair of complex conjugate eigenvalues crossed the imaginary axis, giving rise to a Hopf bifurcation from the limit cycle to the higher energy torus. The real part of the Floquet eigenvalues remains small, thus the limit cycle continues for lower viscosity coefficient as a weakly unstable structure. A second pair of Floquet eigenvalues crosses the imaginary axis at ν_{2cr} near 57 m^2/sec or 58 m^2/sec. This crossing is associated with another bifurcation from the now weakly unstable limit cycle to a lower energy torus. At roughly the same value of ν, a physically similar instability occurs on the higher energy torus. The higher energy torus has a relatively small cross-section and so is "close" to the unstable limit cycle. It is then plausible that the same sort of physical instability should occur on both the limit cycle and the high energy torus. In Figure 14a,b we show Poincaré sections of the unstable limit cycle at $\nu = 60$ and 58 m^2/sec. The section at $\nu = 60$ m^2/sec shows persistent regular divergence from the cycle. In contrast, the section at $\nu = 58$ m^2/sec shows quite irregular divergence from the cycle, which might be an indication of the first and second eigenvalue pair being both close to the imaginary axis. The Hopf bifurcation of the unstable limit cycle may be subcritical, judging by the large amplitude of the lower energy torus at $\nu = 57.7$ m^2/sec, but we do not have enough

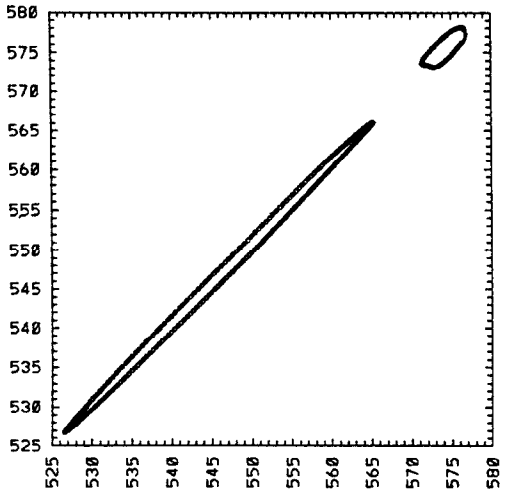

Figure 13. Superimposed Poincaré sections for the higher and lower energy toroidal attractors at ν = 58 m^2/sec and ν = 57.7 m^2/sec respectively.

experiments to conclude this with certainty. More detailed experiments would be expensive computationally.

We have computed a second example on the lower energy branch of toroidal attractors for ν = 57.5 m^2/sec (thus we have two experiments, in which this attractor was found). One difference between the higher energy and lower energy branches of toroidal attractors is the value of the second frequency, associated with a trajectory winding around each of these attractors. The basic periods of both seem similar: 90 days for the higher energy torus at ν = 58 m^2/sec and 86 days for the lower energy torus at ν = 57.5 m^2/sec. This similarity suggests that both tori may arise as bifurcations from the same basic limit cycle solution. However, the second periods are very different, being 420 days for the higher energy torus at ν = 58 m^2/sec and about 9000 days for the lower energy torus at ν = 57.7 m^2/sec (at ν = 57.5 m^2/sec the second period is about 7500 days). This is consistent with the idea that the two tori arose from two *different* Hopf bifurcations of the basic limit cycle. Another possibility is that some sort of global bifurcation has occurred. This second possibility would be the more plausible if the secondary period on the low energy torus tended to infinity as ν was increased above 57.7 m^2/s but it is very difficult to check this. There are types of local bifurcations of a limit cycle that could also introduce a long (initially infinite) period but these are nongeneric and therefore are unlikely to occur in a system like this which lacks spatial symmetries. In Figure 15, we show the power spectrum corresponding to the lower energy torus at ν = 57.7 m^2/sec. Note the appearance near the dominant frequency, $\omega_1 \simeq 0.072$ rad/day, of cross-harmonics with various multiples of the secondary frequency $\omega_2 \simeq 0.0007$ rad/day. How different does the circulation become in physical space when the trajectory leaves the higher energy attractor and winds around the lower energy one? The stream function field experiences a significant change as the trajectory

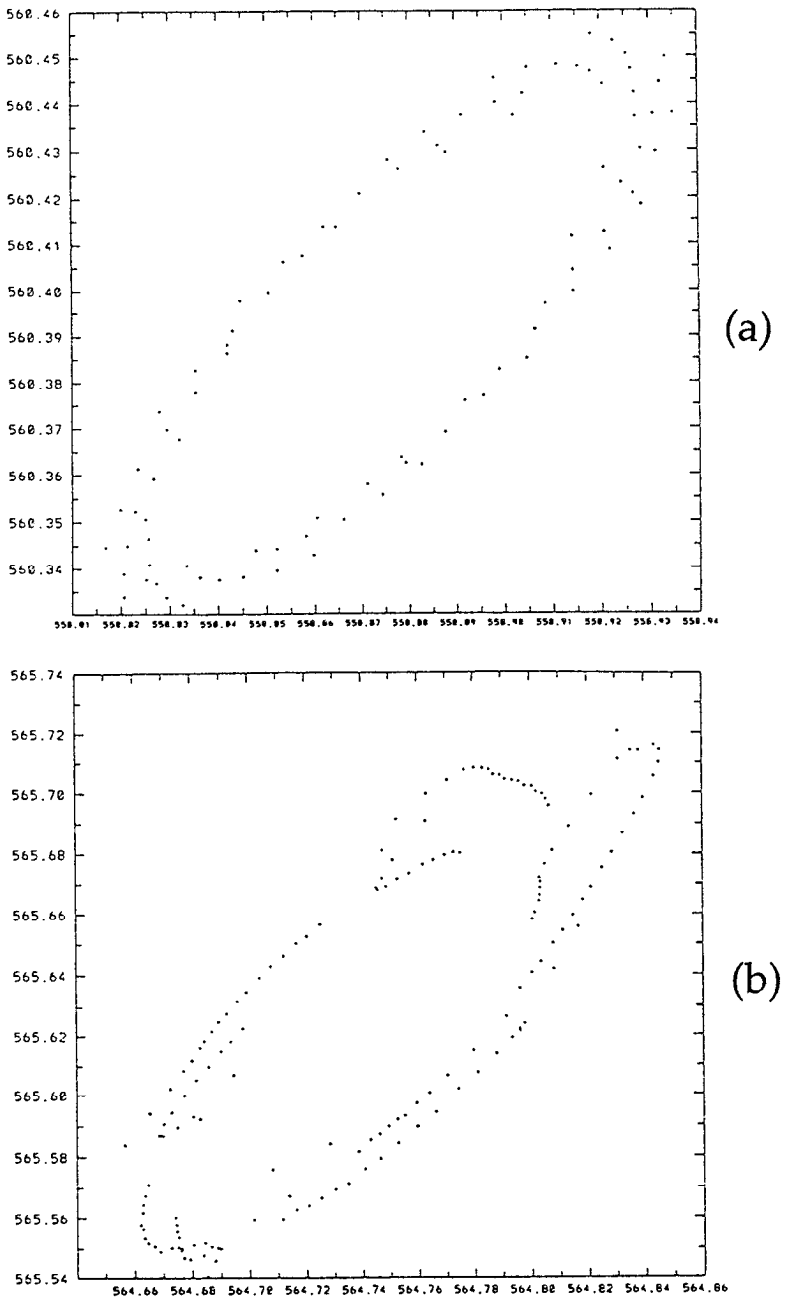

Figure 14. Poincaré sections of the trajectory diverging from the unstable limit cycle at (a) ν = 60 m^2/sec; (b) ν = 58 m^2/scc.

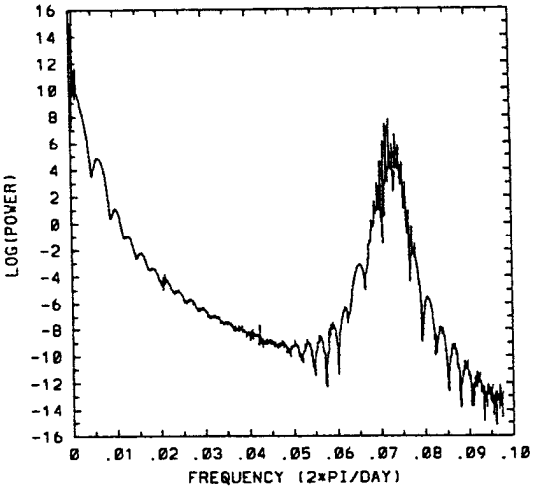

Figure 15. Power spectrum of the energy time series corresponding to a trajectory on the lower energy toroidal attractor at $\nu = 57.7$ m^2/sec. Note two dominant frequencies 0.0007 and 0.072 rad/day (periods are near 9000 and 87 days respectively). The smaller spikes are due to nonlinear interaction between the dominant harmonics.

goes to the lower energy torus; in addition to the three gyres of unequal sizes, which are always present in the time-mean stream function for this set of experiments, the circulation associated with the lower energy torus now exhibits one more time-dependent vortex-gyre in the northern part of the basin between the western and the central gyres. This vortex is present everywhere on the trajectory winding around the lower energy torus, and is a characteristic feature of this attractor. A snapshot of the stream function field for $\nu = 57.5$ m^2/sec is shown in Figure 16; one can see the new recirculation on this picture.

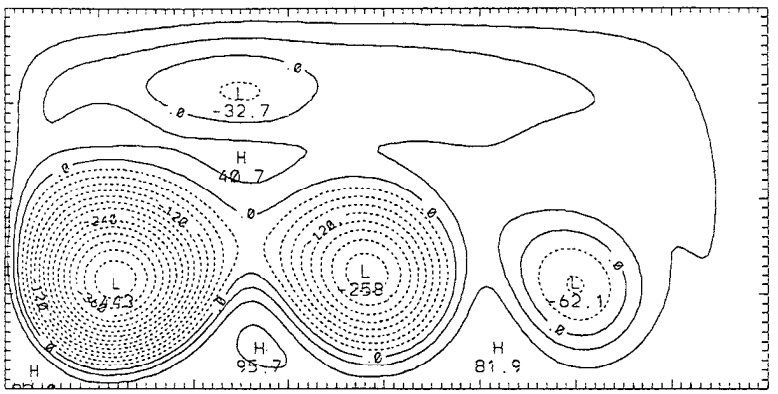

Figure 16. Snapshot of the stream function corresponding to the lower energy toroidal attractor at $\nu = 57.7$ m^2/sec. Note the presence of the permanent recirculation in the northern part of the basin between the western and the central gyres. CI = 30.

It would be useful to determine the physical nature of the secondary instabilities. Unfortunately, this turns out to be a difficult task. In the case of the lower energy torus, one can try averaging the stream function over the short basic period and looking at the differences between these averages and the long-term mean stream function as the center of the averaging window is varied over the period of the secondary oscillation. There are several possible pitfalls in this approach; for example since the "fast" and "slow" oscillations are nonlinearly coupled, the basic period is not uniquely defined locally for windows within the period of the long oscillation. However, given the sharpness of the high frequency spectral peak, it is tempting to try this approach. The result appears to be a standing oscillation at the secondary period in which all three main recirculation gyres oscillate in position, the primary recirculation oscillates in amplitude, and a fourth, oscillatory, zonally elongated recirculation appears in the northern half of the basin. (This fourth recirculation can be seen in the circulation snapshot shown in Fig. 16.) Propagating wave-like disturbances are not seen in the running averages. The origin of this standing oscillation is unknown.

The lower energy toroidal attractor loses stability for $57.3 < \nu < 57.5$ m^2/sec as the result of a new Hopf-like bifurcation. For the attractor found at $\nu = 57$ m^2/sec, we estimated the dimension. We computed the energy time series for a trajectory on the attractor for 10^5 days and estimated the dimension, following the technique described in Section 3. Then, we computed the time series for a further 7×10^4 days and estimated the dimension again, but for the full time series of 1.7×10^5 days. In both cases the dimension was estimated to be between 2.95 and 3.05. The frequencies which predominate in the power spectrum of the time series are shown in Figure 17. The three main frequencies ω are: 0.00095, 0.039 and 0.075 rad/day. The attractor might be a 3-torus, or a strange attractor with a dimension close to 3, but the techniques which we use here fail to distinguish these two possibilities. Figure 18 is a Poincaré section of the attractor, corresponding to $\nu = 57$ m^2/sec. For $\nu = 56$ m^2/sec the attractor's dimension lies between 3.02 and 3.05, a value computed following the same procedure as one described for the attractor at $\nu = 57$ m^2/sec. We show the power spectrum of this attractor in Figure 19. The noninteger dimension suggests the presence of a strange attractor in the system. This is consistent with the appearance of broad band noise in the spectrum. Note especially the red appearance of this spectrum and the significant power seen at decadal time scales. A comparison of the experiments with $\nu = 56$ and 57 m^2/sec suggests that the dimension of the chaotic attractor has a tendency to grow with decreasing viscosity, but the question of for how far in the parameter space the attractor preserves its low-dimensionality is a fairly difficult one and we did not attempt to resolve it.

In Figure 8a, where we plotted the oscillation amplitude versus ν, one can see a sharp increase in amplitude for the high energy toroidal attractors and a very big difference in amplitude between high and low energy toroidal attractors. Another rapid increase in

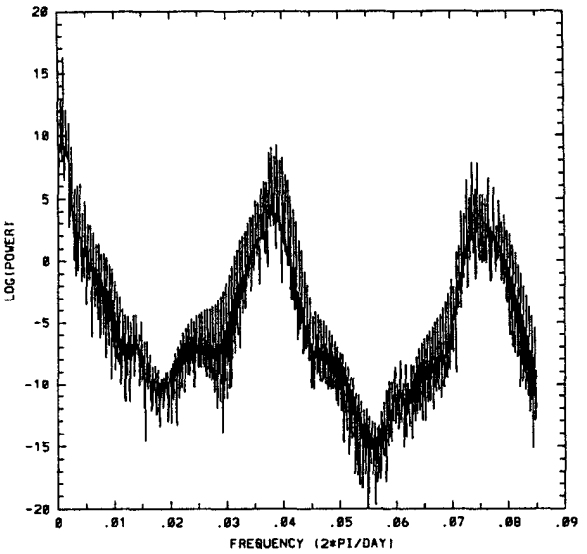

Figure 17. Power spectrum of the time series corresponding to the attractor at $\nu = 57$ m^2/sec. The power is located around 3 frequencies: 0.001, 0.039, 0.075 rad/day (periods are near 6300, 161, 84 days).

amplitude occurs for the 3D attractor. As we pass to the strange attractor, the oscillation amplitude grows to about 14% at $\nu = 56$ m^2/sec (not shown in Fig. 8a).

The sequence of bifurcations which we have seen in our experiments is similar to one of the classical routes to chaos through a sequence of Hopf bifurcations, suggested by Ruelle and Takens (1971) (see also Newhouse *et al.*, 1978; Eckmann, 1981). According to this scenario, quasi-periodic attractors with three or more fundamental frequencies are in general unstable and give way to a strange attractor.

b. Deformation radius as the control parameter. So far, we have considered only the dependence of the bifurcation structure on the single control parameter ν (this corresponds to the nondimensional parameter μ). Ideally, we should try to construct the bifurcation diagram over the full four-dimensional parameter space spanned by (δ, ϵ, μ, S), but this is too expensive computationally. Instead, we carried out a series of computations with fixed $\nu = 100$ m^2/sec, but variable deformation radius Rd (this corresponds to a variation of the nondimensional parameter S). In these experiments, we varied Rd from 20 km to infinity. An infinite Rd corresponds to a purely barotropic model. In that case, $S \equiv 0$. The behavior of a barotropic model is somewhat different from the behavior of the EB model and is discussed in Meacham and Berloff (1997). The average amplitude, frequency and energy of the solutions obtained at various Rd are shown in Figure 20.

When $Rd \leq 20$ km, we found only one steady stable solution, corresponding to a fixed

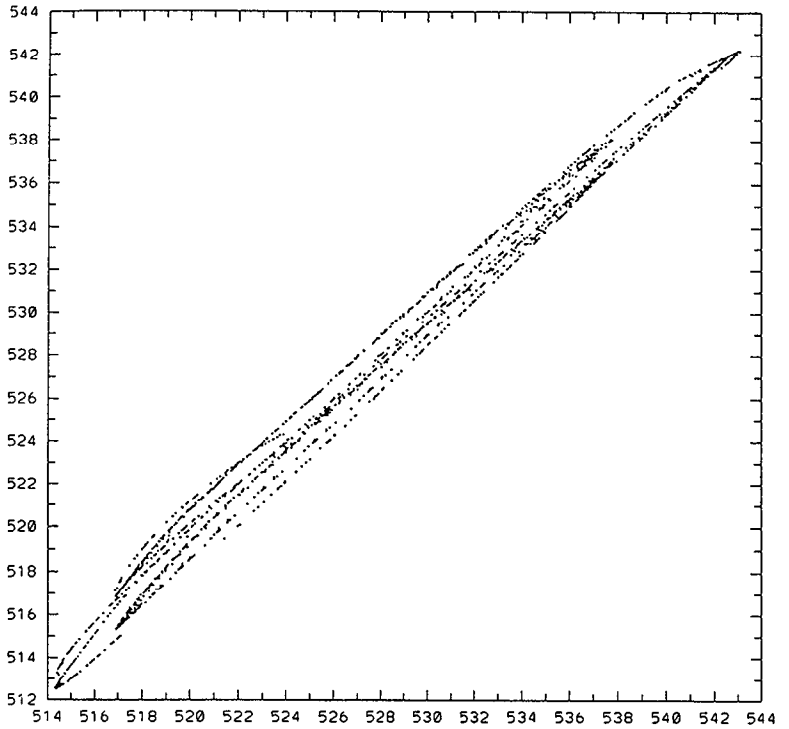

Figure 18. Poincaré section of the attractor at $\nu = 57$ m^2/sec. The dimension estimate of this attractor is very close to 3.

point. This solution exactly coincides with the unstable steady solution, computed above for $\nu = 100$ m^2/sec and $Rd = 24.4$ km. Steady solutions are described by the equation

$$\epsilon J(\psi, \nabla^2\psi) + \frac{\partial \psi}{\partial x} = \nabla \times \tau + \mu \nabla^4 \psi, \tag{10}$$

which does not contain any information about Rd. This means that all steady solutions are exactly the same for any Rd, although the stability properties of the steady solutions depend upon the deformation radius. Multiple steady solutions may be possible, although we could find only one family of stable fixed points.

In the range 22 km $< Rd <$ 22.5 km, the system experiences a supercritical Hopf bifurcation. For the reader's convenience, we'll also quote the numerical values of $s = L_x/Rd = \sqrt{S}$ when describing the sequence of transitions. In particular, $Rd = 22$ km corresponds to $s = 36.36$. The period of the decaying eigenmode for $Rd = 22$ km is 125 days; the period of the growing eigenmode for $Rd = 22.5$ km is 120 days and the period of the small amplitude limit cycle for $Rd = 22.5$ km is 121 days. At $Rd = 24.4$ km ($s = 32.77$) the limit cycle repeats the one from the previous set of experiments, where we varied ν, keeping Rd fixed. The amplitude of the oscillation increases and the basic period

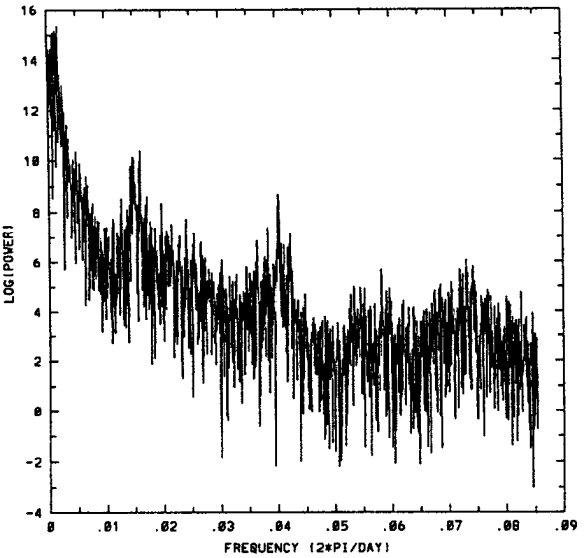

Figure 19. Power spectrum of the time series corresponding to the attractor at $\nu = 56$ m^2/sec. Note the broad and noisy structure of the spectrum.

decreases gradually with increasing Rd as shown on the bifurcation diagrams in Figure 20. This branch of time-dependent solutions experiences a secondary Hopf bifurcation for 56 km $< Rd <$ 57 km ($14.04 < s < 14.29$), which leads to the appearance of a toroidal attractor. We define the basic period of the toroidal attractors on this branch to be the continuation of the periods associated with stable limit cycles. We traced this attractor up to $Rd = 63$ km ($s = 12.70$), but for $Rd = 63.5$ km ($s = 12.60$) it lost stability. The period corresponding to the second dominant frequency on this toroidal attractor decreased from 137 days at $Rd = 57$ km ($s = 14.04$) to 119 days at $Rd = 63$ km ($s = 12.70$). This secondary period is within the range of the periods of the eigenmodes of the unforced basin (Buchwald, 1972). In Figure 21, we show a projection of the toroidal attractor at $Rd =$ 62 km ($s = 12.90$, on the first branch), its Poincaré section and the power spectrum.

A second (or middle) branch of stable asymptotic attractors appeared at $Rd = 56$ km ($s = 14.29$) and ended at $Rd = 75$ km ($s = 10.67$). This is shown with filled circles in Figure 20. Slightly beyond these marginal parameters the attractors belonging to the middle branch lose stability and a trajectory started close to the continuation of the middle attractor converges to an attractor on the first branch (which was the case in the experiment with $Rd = 55.8$ km, $s = 14.34$) or on a third branch (the experiment with $Rd = 75.5$ km, $s = 10.60$), which will be discussed below. With techniques which we use here we are not able to answer the question of whether or not the second branch is a continuation of the first branch. Only computing the unstable time-dependent solutions would allow us to make a conclusion about that. We compared the time-averaged stream functions of the middle branch limit cycles at $Rd = 57$ km ($s = 14.04$) and 72 km ($s = 11.11$) with the first branch

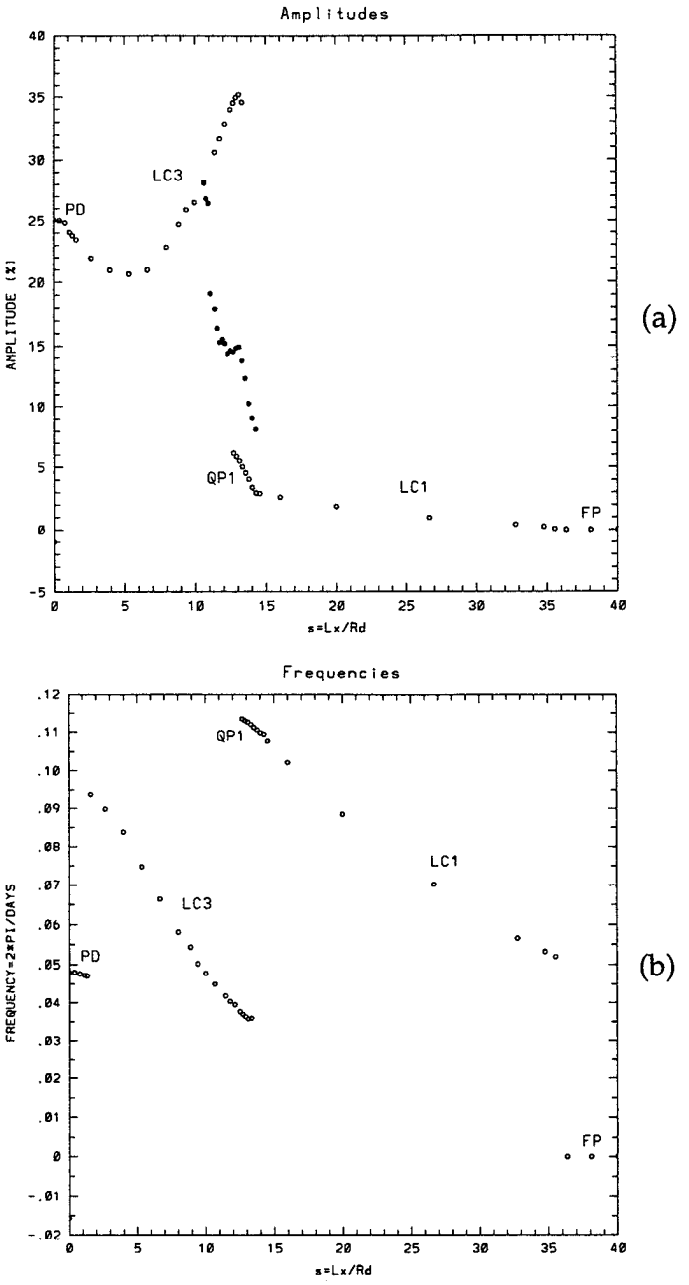

Figure 20. Bifurcation diagram. FP—fixed points; LC1—limit cycle on the first branch of stable attractors; QP1—toroidal attractor on the first branch; LC3—limit cycle on the third branch of stable attractors; PD—limit cycle with doubled period on the third branch. The "middle" branch of attractors is shown with filled circles (see text): (a) The oscillation amplitude as a percentage of mean amplitude versus $s = L_x/Rd$. The primary and the secondary Hopf bifurcations occur approximately at $s = 36$ and $s = 14$ respectively. The period-doubling on the upper branch occurs near $s = 1.45$. (b) The basic frequency of oscillations (only the first and the third branches are shown here) in radian/day versus $s = L_x/Rd$. Note the discontinuities in the frequency at $s = 36$ (the primary Hopf bifurcation) and at $s = 1.45$ (the period-doubling). (c) The mean nondimensional energies of the attractors versus $s = L_x/Rd$.

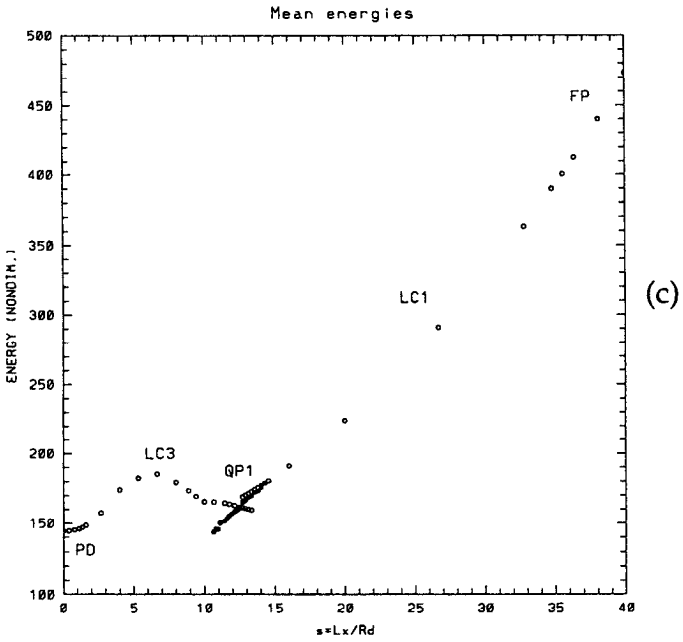

Figure 20. (Continued)

time-averaged stream function at Rd = 55 km or s = 14.55 (the latter stream function is shown in Fig. 24). We found that all three $\langle\psi\rangle$ look qualitatively similar as did the perturbations $\psi'_2 = \psi - \langle\psi\rangle$. This result suggests that the middle branch might be a continuation of the first one.

The results of the experiments on the middle branch are shown in Table 1. From this table, one can see that the middle branch corresponds to a whole variety of topologically different attractors: of 19 experiments, 8 correspond to chaotic attractors, 5 correspond to quasi-periodic attractors, and 6 to phase-locked periodic trajectories on tori. The power spectra for the second branch have several distinctive spikes (see Fig. 22). One intrinsic period in the spectrum decreases with increasing Rd along the middle branch from 140 to 131 days, another increases from 59 to 66 days. A third spike in the spectrum appears near Rd = 60 km (s = 13.33). The period associated with it decreases from close to 1200 to 630 days at Rd = 75 km (s = 10.67). Since the frequencies of the oscillations on the second branch are relatively close to each other in magnitude, the system has a tendency to exhibit a variety of phase-locked orbits (Drazin, 1992). When two of the three dominant frequencies are locked, the attractor becomes toroidal (with quasi-periodic motion on it). The phase locking of all of the dominant frequencies yields a stable limit cycle. An example is the phase locked trajectory for Rd = 68 km (s = 11.76) in Figure 23 (the associated spectrum is shown in Fig. 22c); in this case the frequencies near 0.048 and 0.106 rad/day are locked with the ratio $5/11$, the frequencies near 0.01 and 0.048 rad/day yield the ratio $1/5$ and 0.01, 0.106 rad/day yield the ratio $1/11$. The power spectra for the phase locked and quasi-periodic trajectories have several distinctive spikes with no noisy bands

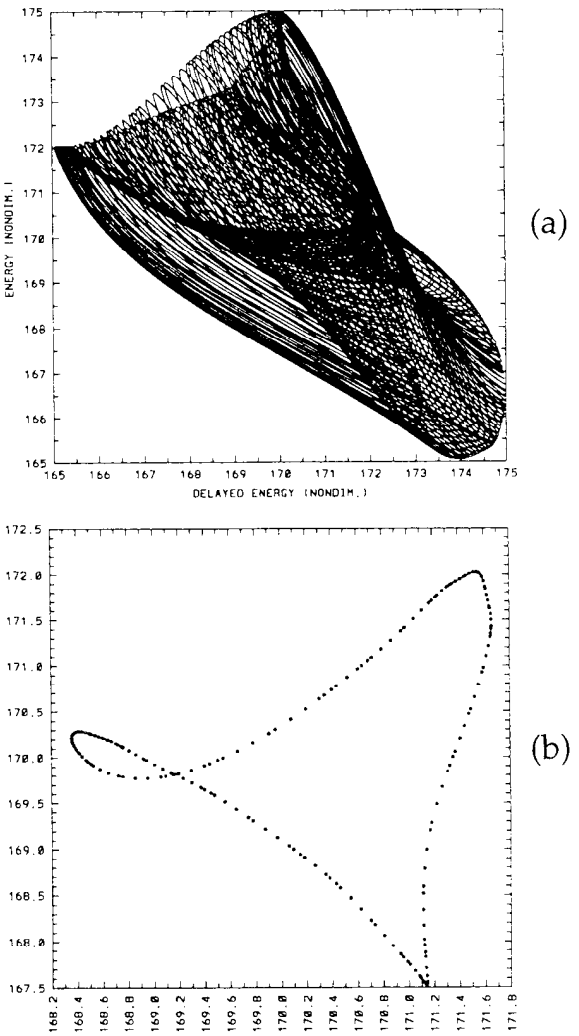

Figure 21. (a) Phase space projection of the trajectory on the toroidal attractor at Rd = 62 km (s = 12.90; an attractor on the first branch); (b) Poincaré section of the trajectory on the toroidal attractor at Rd = 62 km (s = 12.90); (c) Power spectrum of the time series corresponding to the toroidal attractor at Rd = 62 km (s = 12.90). Note two dominant frequencies .052 and .113 rad/day (periods are near 121 and 56 days).

around them; the power spectra for the chaotic attractors have several spikes surrounded by a noisy broad band structure. This noise suggests the presence of a chaotic strange attractor in the system. We estimated the dimensions of the chaotic attractors at Rd = 61 km (s = 13.11) and Rd = 74 km (s = 10.81) from a 1 × 10^5 days long time series, then integrated further in time for .75 × 10^5 days and estimated the dimension from the full time

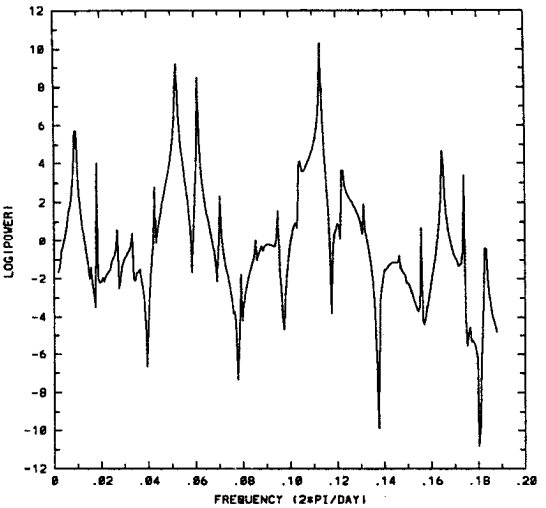

Figure 21. (Continued)

series of 1.75×10^5 days. The longer time series yielded the same dimension estimate as the shorter one. The dimension of the attractor at $Rd = 61$ km ($s = 13.11$) was estimated to be between 3.36 and 3.44. The attractor at $Rd = 74$ km ($s = 10.81$) had a somewhat lower dimension estimated to be between 2.80 and 2.88.

Table 1. Table summarizes the experiments on the middle (the second) branch of stable attractors.

Rd (km)	Regime (with number of basic periods for phase locked orbits)	Amplitude of oscillation (%)
75	chaos	28.1
74	chaos	26.8
73	chaos	26.4
72	phase locking (8)	19.1
70	phase locking (17)	17.9
69	quasi-periodic	16.4
68	phase locking (5)	15.3
67	quasi-periodic	15.5
66	quasi-periodic	15.2
65	phase locking (6)	14.4
64	quasi-periodic	14.6
63	chaos	13.7
62	chaos	14.8
61	chaos	14.9
60	chaos	13.8
59	chaos	12.3
58	phase locking (6)	10.2
57	phase locking (3)	9.07
56	quasi-periodic	8.16

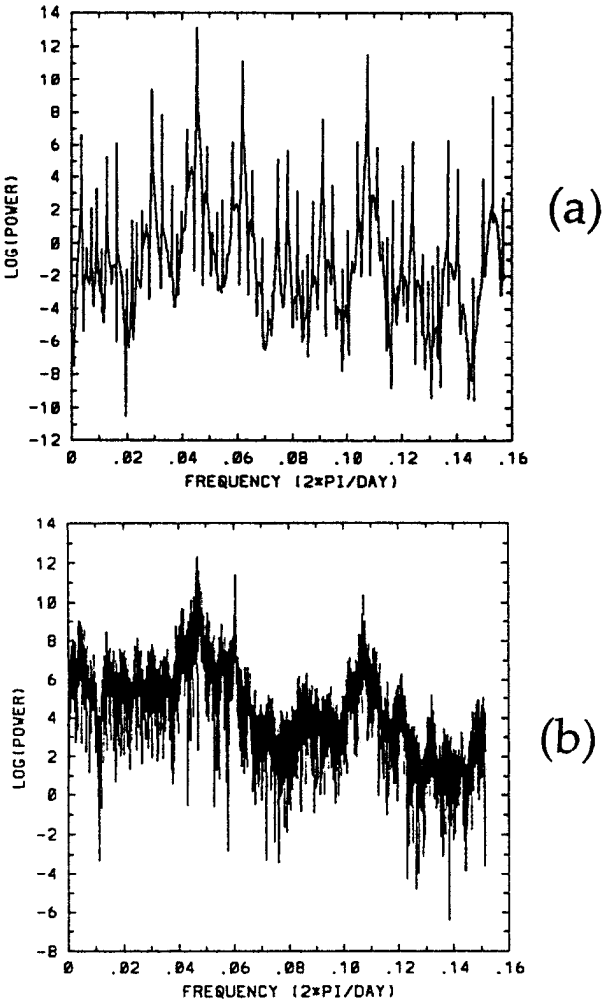

Figure 22. Power spectra of several time series on the middle branch. The attractors are at Rd = 56, 61, 68 and 74 km respectively (s = 14.286, 13.115, 11.765 and 10.811). (a) Quasi-periodic motion on a torus; dominant frequencies are .045 and .107 rad/day (periods are near 140 and 59 days). (b) Power spectrum of a chaotic attractor with a dimension of about 3.4. (c) Power spectrum of a phase locked trajectory on a torus. (d) Power spectrum of a chaotic attractor with a dimension of about 2.8.

A third branch of asymptotic attractors is found at large deformation radii. This branch loses stability for $Rd < 60$ km ($s > 13.33$) so we have not been able to trace it below 60 km, but it continues up to infinite Rd ($s = 0$ in that case and the model is purely barotropic). For 60 km $\leq Rd \leq$ 500 km ($13.33 > s > 1.6$) the attractor on this third branch is a simple limit cycle. We computed time-averages over one period for two limit cycles; one, corresponding to Rd = 55 km (s = 14.55), lies on the first branch of attractors, the

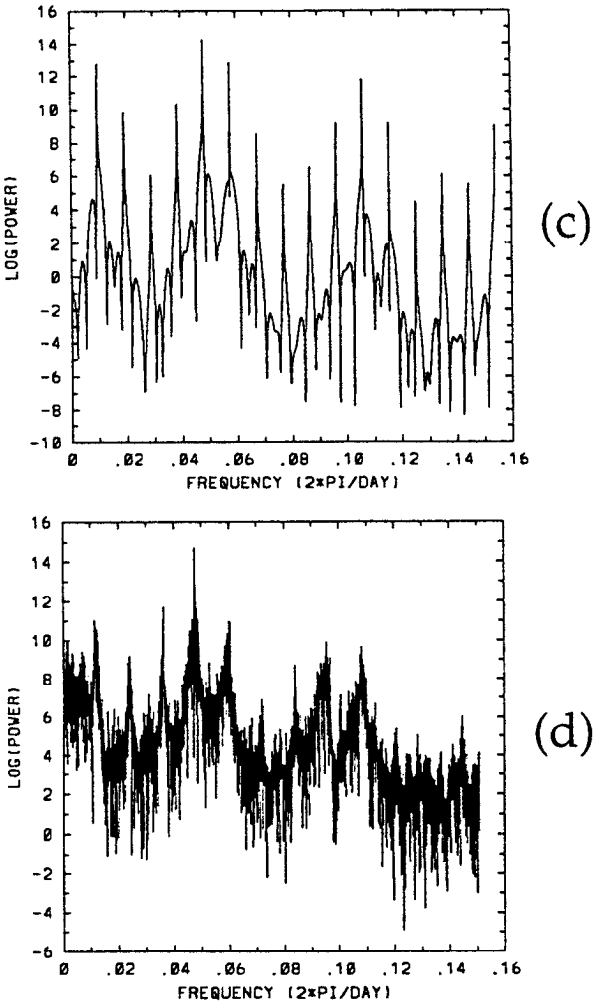

Figure 22. (Continued)

second, with $Rd = 60$ km ($s = 13.33$), lies on the third branch (Figure 24). One can see that the main difference between the average flows is the appearance/disappearance of a third (eastern) gyre. In the limit cycle on the third branch, the circulation develops only two relatively weak gyres, whereas on the first branch we observe three, more intense, gyres in the time-mean flow. The limit cycle on the first branch at $Rd = 55$ km ($s = 14.55$) looks qualitatively similar to the limit cycle computed at $\nu = 75$ m^2/sec and $Rd = 24.4$ km ($s = 32.79$) in the set of experiments with variable ν, and shown in Figure 7c. The third branch limit cycle oscillations at $Rd = 60$ km ($s = 13.33$) are quite different. In Figure 25, we show deviations from the mean, ψ'_2, on this limit cycle. The perturbations in this case occupy the whole basin and not the western part of it as on the first branch. The third branch

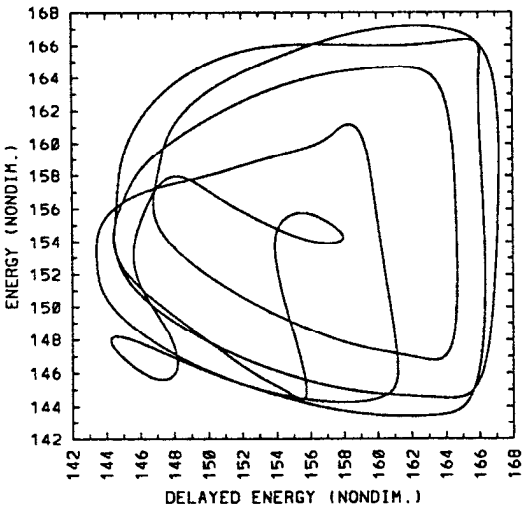

Figure 23. Example of a phase locked trajectory at Rd = 68 km (s = 11.765; the middle branch of attractors).

oscillation pattern is not a basin mode (c.f. Pedlosky, 1987), although it has a basin-filling structure. The frequency of the limit cycle on this branch is about twice as large as the frequency of the gravest basin mode. The third branch oscillation pattern seems to be similar to the one found by Meacham and Berloff (1997) in the barotropic case ($Rd \rightarrow \infty$).

The third branch of asymptotic attractors exhibits a subharmonic bifurcation at some critical value of Rd between 500 and 600 km ($1.33 < s < 1.60$). This corresponds to a *period-doubling* instability (Drazin, 1992). If a Floquet multiplier decreases through -1, when the control parameter passes through a critical value, the system experiences a subharmonic instability, and there is a doubling of the period of the attracting limit cycle. This is very apparent in delay coordinate phase space where the orbit develops a characteristic double-looped structure. The period-doubled limit cycle attractor for Rd = 700 km (s = 1.14) is shown in Figure 26. For $Rd \rightarrow \infty$ ($s \rightarrow 0$) the period and amplitude of oscillations asymptote to constant values. The physics behind the period-doubling in the model remains to be explained.

5. Conclusions and discussion

The work in this paper complements previous studies of the wind-driven circulation (Bryan, 1963; Veronis, 1966; Ierley and Sheremet, 1995; Jiang *et al.,* 1995; Cessi and Ierley, 1995; Speich *et al.,* 1995). By focusing on a relatively small oceanic basin with a size comparable to the Black Sea, we have been able to run the model repeatedly at different parameter values for a sufficiently long time that the underlying dynamical behavior of the model becomes strikingly apparent. Viewed as a dynamical system, the EB general circulation model (GCM) can be considered as a large-dimensional forced and

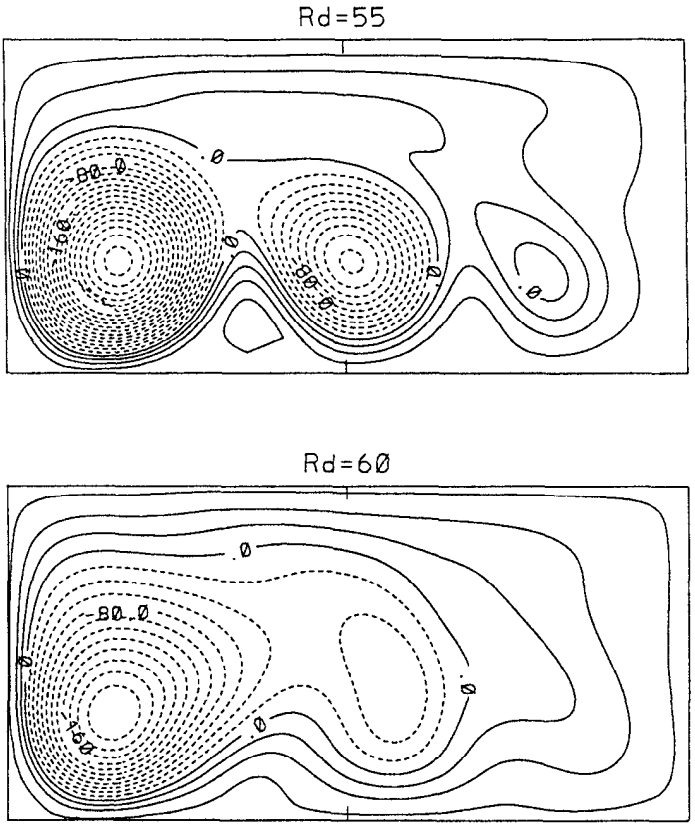

Figure 24. Time-average over one limit cycle of the stream functions (a) at $Rd = 55$ km ($s = 14.545$) on the first branch of the attractors and (b) at $Rd = 60$ km ($s = 13.333$) on the third branch. Note, that the recirculation gyres are weaker at $Rd = 60$ km ($s = 13.333$) and the third (eastern) recirculation is not present in the time-average. CI = 20.

dissipative dynamical system with several control parameters representing forcing, dissipation and the internal deformation radius of the problem. For a wide range of the parameters, including values of the viscosity coefficient widely used in modern GCMs, and values of the deformation radius including those estimated for the Black Sea, the system possesses a sequence of low-dimensional attractors. To identify those attractors we applied a *delayed coordinate* technique. Following this technique we synthesized low-dimensional projections of the full phase space. Integrating the model in time from some initial conditions, we observed that the phase space trajectory asymptotes to attracting sets of rather low dimensions, with structures that depend upon the control parameters. Motion on each of the unsteady asymptotic attractors corresponds to a time-dependent circulation with one, two or three dominant intrinsic time scales. These time scales range from months to decades. The low-dimensionality of the formally large-dimensional system is persistent for a wide range of parameters and seems to be a robust feature of this wind-driven circulation model.

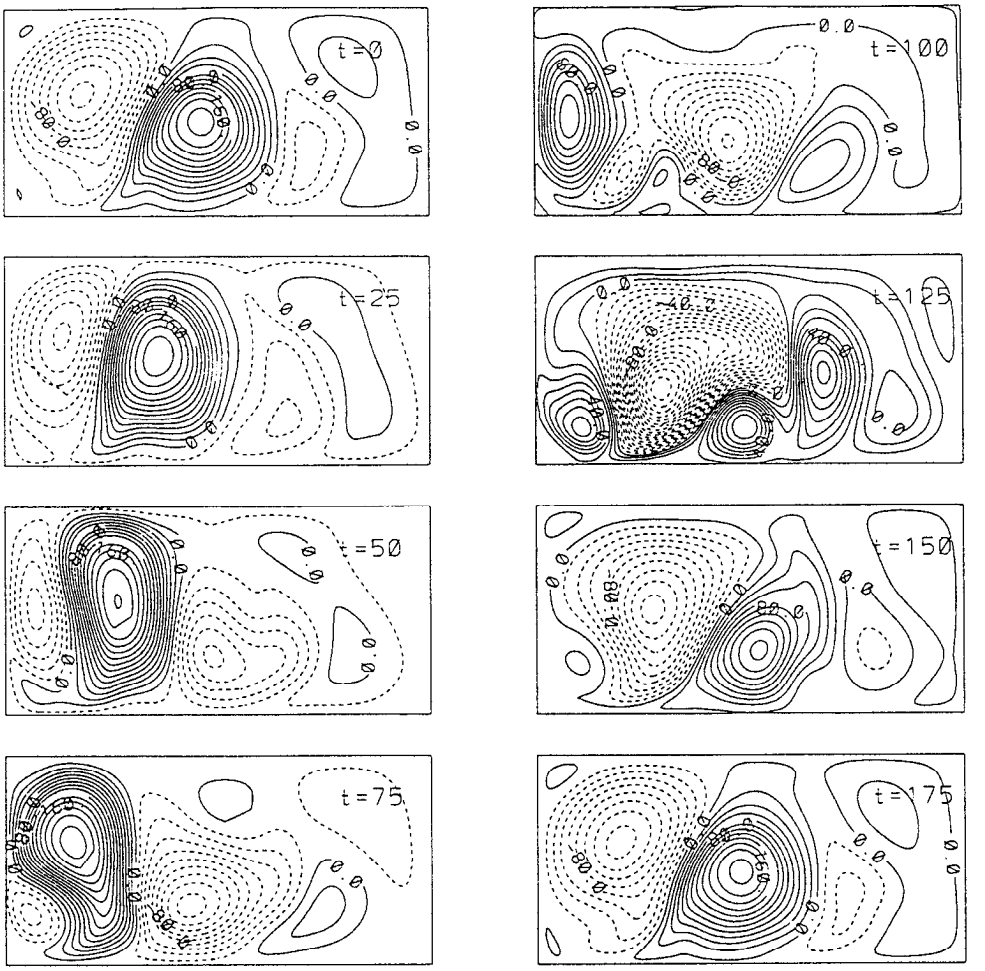

Figure 25. Behavior of the circulation over the limit cycle at ν = 100 m^2/sec and Rd = 60 km (s = 13.333). The evolution of the difference between the instantaneous and the average stream functions. Time t is measured in days. CI = 20.

This is consistent with the ideas of Lions *et al.* (1992) who showed that, under certain assumptions, the time-dependent behavior of an oceanic primitive-equation model ought to asymptote to motion on a finite-dimensional invariant set in phase space.

Varying the viscosity coefficient in one set of experiments, and the internal deformation in another, we observed two sequences of successive bifurcations in the system. Each bifurcation was associated with a change in the attractor topology, i.e. with a change in the structure of the time-dependent solution to which the model asymptotes. The bifurcation sequence seen when the viscosity coefficient was varied was similar to a classical Ruelle-Takens scenario for a transition to chaos. The attractor that we found for a value of

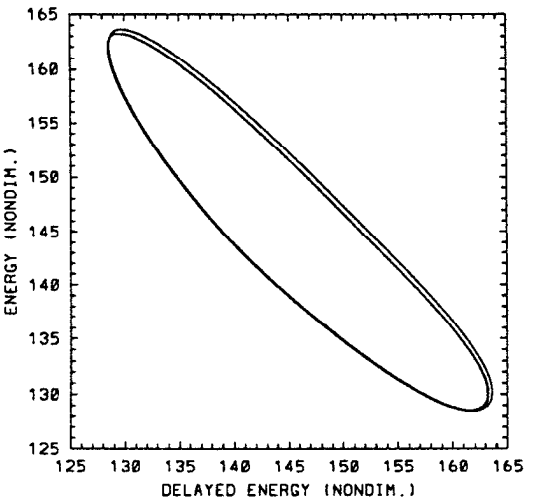

Figure 26. Period-doubled trajectory at a value of Rd = 700 km (s = 1.143), which is close to the period doubling bifurcation point.

the viscosity coefficient just below the critical value associated with the third in a sequence of Hopf bifurcations had a dimension very close to three, and the dimension seemed to grow as the viscosity coefficient was reduced further.

In the set of experiments with variable deformation radius, we found ranges of that parameter where two or three different, stable, time-dependent attractors coexist. This sequence also includes a period-doubling on one branch of attractors, transition to a quasi-periodic motion on a torus on another branch, and a stable fragment of a third branch, rich in phase lockings, quasi-periodic and chaotic attractors. The existence of parameter regimes in which multiple stable time-dependent attractors occur is a significant result. In a situation where similar multiple time-dependent equilibria exist but are weakly unstable, one might anticipate that models will exhibit multiple persistent regimes such as those found by McCalpin and Haidvogel (1996). The situation in which the multiple equilibria are stable, as here, raises the question of what sort of transient external perturbations can cause the system to switch from one equilibrium to another. This will be a difficult question to answer coherently because of the many possible forms a transient perturbation can take. Though the attractors themselves are low-dimensional, they are embedded in the high-dimensional full phase space of the model. Their basins of attraction are high-dimensional objects in this phase space.

When compared to simulations and observations of the Black Sea, in the range of the control parameters which we explored, the time-dependent circulation contains recirculation gyres, but does not contain a Rim Current. Berloff and Meacham (1997b) have considered a simple baroclinic model of the wind-driven circulation in the same basin. This too exhibits bifurcation sequences characteristic of low-dimensional behavior. However, in

the baroclinic model, the character of the circulation in physical space is closer to that observed in the Black Sea and includes a reasonable Rim Current.

The nature of the primary instability, associated with a Hopf bifurcation, is examined through a consideration of the energetics of the most unstable linear eigenmode of the steady state flow. The instability appears localized in the western boundary intensification, the western gyre and the meander between the western and the central gyres.

Any GCM is a forced and dissipative system, and any GCM contains nonlinearity and mechanisms for internal instabilities. We conjecture that the presence of low-dimensional stable attractors for some range of the parameters is a robust feature of GCMs with steady forcing. This would be consistent with general results for forced dissipative PDE's discussed by Robinson (1995), Lions *et al.* (1992) amongst others. Similar attractors were found in barotropic (Meacham and Berloff, 1997), baroclinic (Berloff and Meacham, 1997a) and 1.5-layer shallow-water (Speich *et al.*, 1995) models of the wind-driven circulation, and in a two-dimensional model of the thermohaline circulation (Quon and Ghil, 1996). On the basis of these results, it is plausible that, while realistic topography, coastline, stratification, steady heat and freshwater fluxes will modify attractors and the convergence rate to them, the existence of low-dimensional attractors will be a persistent feature of such models for a significant parameter range. One potential effect of adding topography might be to tend to decouple parts of the ocean basin; thus, it may be possible to find spatio-temporal chaos as well as temporal chaos in such a model.

Qualitatively different behavior of the circulation may be observed, if time-dependence is added to the forcing. In general, we expect that realistic time-dependent forcing in GCMs will prevent complete convergence to a low-dimensional attractor, but in some circumstances the circulation will seek to stay "close" to the attractor. In that case, the attractor may be a statistically preferred state of the system, and the underlying organized patterns and temporal variability associated with the attractor may be present in the flow. This statistical presence of the low-dimensional characteristics may be an explanation of the organized Gyres and the Rim Current in the Black Sea. In situations where the time-dependence of the forcing is simply periodic, the time dependence of the forcing can be folded into the dynamical system of the model by adding a degree of freedom that is just a constant amplitude oscillator. In this case, a range of transitions through low-dimensional attractors should be seen in much the same way as in the constantly forced models. The main difference will be that in the strongly dissipative limit, the initial attractor will be a limit cycle rather than a fixed point.

The intrinsic temporal variability associated with the presence of the underlying low-dimensional attractors may exhibit itself on interannual-to-decadal time scales, and should be distinguished from the seasonal and annual cycles imposed by the atmospheric forcing. A significant and robust feature of the bifurcations to chaotic attractors seen in this study is the concomitant appearance of spectral power at long (interannual-to-decadal) time scales. It seems important, when trying to understand the behavior of ocean models on "climatological" time scales, to investigate this intrinsic source of low-frequency variabil-

ity in more detail and, in particular, to try and tie the geometrical structure of the attractors in phase space to physical processes occurring within the flow. The existence of a natural internal mechanism for the generation of long time scale fluctuations is something that must be taken into account when considering climatological behavior. For similar reasons, but a rather more difficult task, it would be worthwhile to explore the way in which the structure of the chaotic attractors seen in this study change as dissipation is reduced further. Such changes are likely to affect the distribution of energy at long time scales (see Meacham and Berloff, 1997), the length of the "longest" time scale, and the existence and form of persistent states within the chaotic regime.

Meacham and Berloff (1997) showed that, in the barotropic wind-driven model flow, energy is predominantly dissipated in thin regions located along the western wall of the basin and at the southern edge of the western recirculation gyre. The thinness of these regions is scaled by the width of viscous boundary layer δ_M and requires relatively high resolution. Meacham and Berloff studied the effect of resolution on the bifurcation sequence. They showed that for higher resolution, the primary bifurcation threshold shifted slightly to a higher value of ν and mean energies of the attractors in the bifurcation sequence increased slightly, but the bifurcation sequence qualitatively did not change. For the EB model, we changed the resolution from 6.25 km to 3.125 km and halved the time step, keeping $Rd = 24.4$ km, and found that, instead of $\nu = 104$ m^2/sec, the primary bifurcation occurred at a higher value of ν, somewhere between 109 and 112 m^2/sec. We also computed the limit cycle at $\nu = 80$ m^2/sec and $Rd = 24.4$ km, and found that, when compared to the 6.25 km resolution case, the mean energy of the limit cycle grew by 4% and the period changed by less than 1%. These results, as well as those of Meacham and Berloff (1997), suggest that under-resolving the western boundary layer may cause the circulation to equilibrate at a lower energy level.

We hope that, with the growing evidence of the organized low-dimensional behavior in ocean models, a combination of systematic studies with the dynamical system approach applied to more realistic models and observations of the real ocean will lead to a better understanding of the ocean's spatio-temporal variability.

Acknowledgments. This work was supported by the National Science Foundation (grant OCE-9301318). We are grateful to Drs. N. Balmforth, K. Julien and E. Spiegel for useful discussions on the topics of bifurcations. We also wish to thank E. Kostelich for the numerical code for the fractal dimension estimate.

REFERENCES

Arakawa, A. 1966. Computational design for long-term integration of the equations of fluid motions. J. Comp. Phys., *1,* 119–143.

Badii, R. and A. Politi. 1985. Statistical description of chaotic attractors: the dimension function. J. Stat. Phys., *40,* 725–750.

Berloff, P. and S. Meacham. 1997a. The dynamics of a simple baroclinic model of the wind-driven circulation. J. Phys. Oceanogr., (submitted).

—— 1997b. On the stability of equivalent-barotropic and baroclinic models of the wind-driven circulation. J. Mar. Res., (submitted).

Blatov, A., N. Bulgakov, V. Ivanov, A. Kosarev and V. Tuzhilkin. 1984. Variability of the Black Sea Hydrophysical Fields, B. Nelepo, ed., Leningrad Gydrometeoizdat, 240 pp. (in Russian).

Brandstater, A. and H. L. Swinney. 1987. Strange attractors in weakly turbulent Couette-Taylor flow. Phys. Rev. A, *35,* 2207–2220.

Bryan, K. 1963. A numerical investigation of a nonlinear model of a wind-driven ocean. J. Atmos. Sci., *20,* 594–606.

Buchwald, V. 1972. Long period divergent planetary waves. Geophys. Fluid Dyn., *5,* 359–367.

Cessi, P. and G. Ierley. 1995. Symmetry-breaking multiple equilibria in quasi-geostrophic wind-driven flows. J. Phys. Oceanogr., *25,* 1196–1205.

Drazin, P. 1992. Nonlinear Systems. C.U.P., Cambridge, 317 pp.

Eckmann, J.-P. 1981. Roads to turbulence in dissipative dynamical systems. Rev. Modern Phys., *53,* 643–654.

Farmer, J., E. Ott and J. Yorke. 1983. The dimension of chaotic attractors. Physica D, *7,* 153–180.

Figueroa, H. and D. Olson. 1994. Eddy resolution versus eddy diffusion in a double gyre GCM. Part I. J. Phys. Oceanogr., *24,* 371–402.

Fraser, A. M. and H. L. Swinney. 1986. Independent coordinates for strange attractors from mutual information. Phys. Rev. A, *33,* 1134–1140.

Hockney, R. 1970. The potential calculation and some applications. Methods in Comput. Phys., *9,* 136–211.

Ierley, G. and V. Sheremet. 1995. Multiple solutions and advection-dominated flows in the wind-driven circulation. Part I: Slip. J. Mar. Res., *53,* 703–737.

Ierley, G. and W. Young. 1991. Viscous instabilities in the western boundary layer. J. Phys. Oceanogr., *21,* 1323–1332.

Jiang, S., F. Jin and M. Ghil. 1995. Multiple equilibria, periodic, and aperiodic solutions in a wind-driven, double-gyre, shallow-water model. J. Phys. Oceanogr., *25,* 764–786.

Kamenkovich, V. and I. Kamenkovich. 1993. On the evolution of Rossby waves, generated by wind stress in a closed basin, incorporating total mass conservation. Dyn. Atmos. Oceans, *18,* 67–103.

Kostelich, E. 1990. Software for calculating attractor dimension using the nearest neighbor algorithm with accompanying text. Available by anonymous ftp (eric@chaos.utexas.edu).

Kostelich, E. and H. Swinney. 1987. Practical considerations in estimating dimension from time series data, *in* Chaos and Related Nonlinear Phenomena, I. Procaccia and M. Shapiro, eds. Plenum Press, New York.

Lions, J.-L., R. Temam and S. Wang. 1992. On the equations of the large-scale ocean. Nonlinearity, *5,* 1007–1053.

Marshall, J. and G. Nurser. 1986. Steady, free circulation in a statistical quasi-geostrophic ocean. J. Phys. Oceanogr., *16,* 1799–1813.

McCalpin, J. and D. Haidvogel. 1996. Phenomenology of the low-frequency variability in a reduced-gravity, quasi-geostrophic double-gyre model. J. Phys. Oceanogr., *26,* 739–752.

Meacham, S. 1997. The response of a small basin circulation to variations in forcing. J. Phys. Oceanogr. (submitted).

Meacham, S. and P. Berloff. 1997. Barotropic wind-driven circulation in a small basin. J. Mar. Res., *55,* 523–563.

Munk, W. 1950. On the wind-driven ocean circulation. J. Meteorol., *7,* 79–93.

Newhouse, S., D. Ruelle and F. Takens. 1978. Occurrence of strange axiom *A* attractors near quasi periodic flows on T^m, $m \geq 3$. Commun. Math. Phys., *64,* 35–40.

Oguz, T., V. Latun, M. Latif, V. Vladimirov, H. Sur, A. Markov, E. Ozsoy, B. Kotovshchikov, V. Eremeev and U. Unluata. 1993. Circulation in the surface and intermediate layers of the Black Sea. Deep-Sea Res., *40,* 1597–1612.

Packard, N., J. Crutchfield, J. Farmer and R. Shaw. 1980. Geometry from a time series. Phys. Rev. Lett., *45,* 712–716.

Pedlosky, J. 1987. Geophysical Fluid Dynamics. 2nd ed., Springer-Verlag, New York, 710 pp.

Quon, S. and M. Ghil. 1996. Successive bifurcations and stable oscillations in 2-D thermohaline convection. (In preparation).

Robinson, J. 1995. Finite-dimensional behavior in dissipative partial differential equations. Chaos, *5,* 330–345.

Ruelle, D. and F. Takens. 1971. On the nature of turbulence. Commun. Math. Phys., *20,* 167–192.

Speich, S., H. Dijkstra and M. Ghil. 1995. Successive bifurcations in a shallow-water model applied to the wind-driven ocean circulation. Nonlin. Proc. Geophys., *2,* 241–268.

Stanev, E. 1990. On the mechanisms of the Black Sea circulation. Earth-Science Rev., *28,* 285–319.

Stommel, H. 1948. The westward intensification of wind-driven oceanic currents. Trans. Am. Geophys. Union, *29,* 202–206.

Takens, F. 1981. Detecting strange attractors in turbulence, *in* Dynamical Systems and Turbulence, D. Rand and L.-S. Young, eds., Springer-Verlag. Lecture notes in Math., *898,* 366–381.

Temam, R. 1995. Navier-Stokes Equations and Nonlinear Functional Analysis. 2nd ed., CBMS-NSF regional conference series in applied mathematics, *66.* SIAM, Philadelphia. 141 pp.

Veronis, G. 1966. Wind-driven ocean circulation. Part 2. Deep-Sea Res., *13,* 31–55.

Whitney, H. 1936. Differentiable manifolds. Ann. Math., *37,* 645–680.

Received: *25 March, 1996;* revised: *17 December, 1996.*